'An Instrument to Study Computed Tomography Using Microwaves'

by

Pierre Michel Forgues

A Thesis
presented to the University of Ottawa
in partial fulfillment of the
requirements for the degree of
Master of Applied Science
in
Department of Electrical Engineering

Ottawa, Ontario, 1980

I hereby declare that I am the sole author of this thesis.

I authorize the University of Ottawa to lend this thesis to other institutions or individuals for the purpose of scholarly research.

Pierre Michel Forgues

I further authorize the University of Ottawa to reproduce this thesis by photocopying or by other means, in total or in part, at the request of other institutions or individuals for the purpose of scholarly research.

Pierre Michel Forgues

The University of Ottawa requires the signatures of all persons using or photccopying this thesis. Please sign below, and give address and date.

ABSTRACT

This thesis presents a discussion of state of the art in Computed Tomography (CT) technology followed by the introduction of an alternate approach using microwaves.

The mathematical and physical principles of CT are presented. The properties of X-rays and ultrasound for the purpose of reconstruction are given.

This is followed by a discussion of the merits of electromagnetic (EM) waves in the microwave portion of the spectrum as interrogating waves. The use of a parallel-plate chamber to study the scattering of EM waves from objects of arbitrary composition is examined.

Following this is a presentation of the actual design procedure and final configuration of an instrument used to measure fields scattered from objects. Preliminary results obtained using the instrument are presented and interpreted as a function of the relative importance of refraction and diffraction on the total field.

ACKNOWLEDGEMENTS

The author wishes to express his deepest gratitude to his thesis supervisors, Professors Morris Goldberg and Stan Stuchly, for their encouragement and guidance throughout this work.

Special thanks are also due to Andy Smith for his invaluable help, ranging from workshop interfacing to stimulating discussions on the physical principles of diffraction.

The author also wishes to express his appreciation to all members of the EE department, especially Mohammed Masters, Ben Carrarro and Steve Symmons for their help associated with various parts of the project.

Thanks to the National Research Council and to the University of Ottawa for financial assistance throughout the duration of the work. Thanks are also due to the Ontario Ministry of Labour (Grant 095/R) for the funding of the project.

LIST OF ACRONYMS

AGN	Additive Gaussian Noise
ART	Algebraic Reconstruction Technique
CAT	Computer Assisted Tomography
CT	Computed Tomography
CTAT	Computerized Transverse Axial Tomography
DSR	Dynamic Spacial Reconstructor
ECT	Emission Computed Tomography
EMI	Electronic Music Instruments Limited
MCT	Microwave Computed Tomography
RT	Reconstruction Tomography
SIRT	Simultaneous Iterative Reconstruction Technique
TOF	Time of Flight
UCT	Ultrasonic Computed Tomography

TABLE OF CONTENTS

LIST OF TABLES

LIST OF FIGURES

Chapter I

INTRODUCTION

This chapter contains the motivation, a statement of the problem and an outline of the thesis.

1.1 THE MOTIVATION

The ability to view internal structures non-destructively has long been a goal in many fields such as medicine, geology, and engineering physics. Advances towards this goal have been achieved in many of those disciplines; but none was as fast and as explosive as the development of a new technique known as Computer Aided Tomography (CAT) in medicine. The benefits obtained using this technique are demonstrated by the clinical usefulness of many X-ray CAT machines presently in operation.

There is growing interest in the investigation of the use of electromagnetic radiation in these fields of science. The two-dimensional inverse scattering problem has been studied extensively, particularly for target recognition using radar and sonar. However, reconstructions using this concept are not available in open literature, but it is

quite possible that advances have been made in military applications such as target shape estimation.

The greatest motivation for the investigation of microwaves in computed tomography is that it has never been attempted in the past. Perhaps more information can be gained with their use; for example, soft tissue in the human body frequently provides little contrast for X-rays; but possibly higher contrast can be obtained using microwaves. Also, the ability to sweep the source over a wide range of frequencies may give additional insight on wave propagation in arbitrary media. The need to study this area further is the very incentive for this research.

1.2 THE PROBLEM

Three major tomographic imaging modalities have already been studied extensively; namely, X-ray transmission, radiation emission and ultrasound. All methods share the same goal: the reconstruction of a quantitative cross-sectional image of the internal structure of an unknown sample. The final display obtained is a map of some property of the interrogating wave in the medium. Reconstruction using X-rays and emission of radiation is relatively easy by the very nature of these waves as will be seen later. Ultrasound tomography is more difficult due to the increased effects of refraction and finally, microwaves

pose even further difficulties due to the combined effects of refraction and diffraction.

The scattered fields examined here come from objects made of conducting or dielectric materials. These objects are irradiated with a uniform plane transverse electromagnetic (TEM) wave and the forward scattering is measured. Several projections are obtained by repeating the procedure in many directions. From this projection data, an estimation of the size, shape and composition of the object is obtained by reconstructing its internal dielectric properties using a digital computer.

1.3 OUTLINE

This thesis deals with the design and testing of an instrument to be used to study microwave computed tomography (MCT).

The second chapter introduces the work previously done in computed tomography, its scientific principles, reconstruction algorithms and scanning geometries. This is followed by a chapter on previous work in microwave imaging. The fourth chapter presents the design criteria and the configuration of the final instrument built and tested in the course of this investigation. This is followed by a chapter that summarizes the experimental results obtained

with the instrument. The last chapter of this thesis deals with possible future directions and conclusions. Two appendices are also included to present the derivation of the expression for scattering from metal cylinders and for additional results.

Chapter II

REVIEW OF COMPUTED TOMOGRAPHY

Computed Tomography (CT) is revolutionizing the field of radiology and has proven useful in other areas such as geology, radioastronomy and electron microscopy [28],[6],[13]. The word tomography comes from the greek words tomos meaning "section" or "slice" and graphy meaning "to write". The technique known as computed tomography consists in reconstructing a plane of an unknown object from projections taken at different angles. These projections are measurements of a transformation, such as attenuation, that an "interrogative wave" undergoes as it propagates through the object. Because these projections are taken on the opposite side of the object from the source, they are also called shadows or signatures of the object.

This chapter describes the evolution of this technique, its mathematical and physical principles as well as a few reconstruction algorithms.

2.1 SHORT HISTORY OF COMPUTED TOMOGRAPHY

The historical development of tomography has paralleled the development of X-rays [34]. It started in 1895 when Roentgen discovered the effect of X-rays on unexposed photographic film. Within nine months, photographic records of the interior of the human body were produced in many laboratories. These photographs were just maps of the attenuation of X-rays in the body along the direction of propagation; each direction being one projection or shadow. The major problem encountered in early radiology was that all internal structures were superimposed on one another in the resulting image.

In 1921, Bocage introduced focal-plane tomography to alleviate this problem. This is an X-ray transmission technique which images a particular plane in the patient's body (plane B'-B" in Fig. 1). The X-ray source and film are moved along special trajectories so that only the desired plane (B'-B") remains in focus, while the others are blurred. Although focal-plane tomography emphasizes the desired plane, the final image still contains all the blurred planes superimposed on it.

The mathematical foundations of true tomography were established by J. Radon in 1917. He demonstrated that an object could theoretically be reconstructed from an infinite

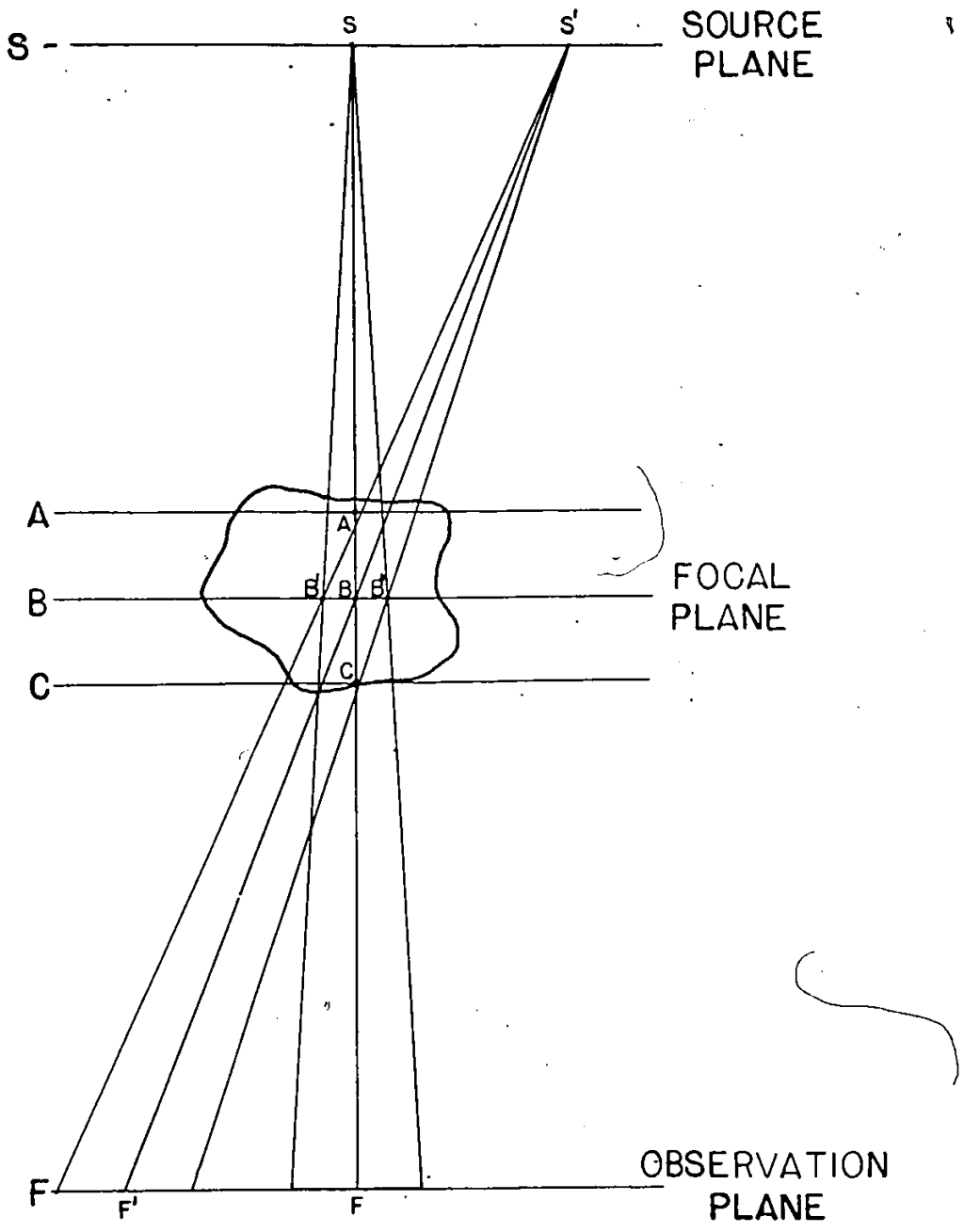

Figure 1: Focal-Plane Tomography

number of its projections or line integrals. Combined with Roentgen's discovery, it would have been sufficient for the development of a CAT scanner, but a half century interlude passed before the advent of high speed digital computers made this undertaking practically feasible.

The first reconstructions from projections were performed in 1956 by Bracewell [6]. He developed his technique for reconstruction in radioastronomy. The purpose was to make a map of the regions of the sun which emit microwave radiation. The radio-astronomical observations made gave only the intensity along strips of the sun; that is along projections or line integrals over the surface of the sun. By taking strip measurements from many directions followed by a little processing, he showed that the true distribution of microwave sources can be recovered.

After Bracewell's work, several researchers involved in medicine experimented with the principle of projections. Takahashi worked on X-ray tomography in 1957, Oldendorf used gamma-ray transmission in 1961, followed by the work of Kuhl (1963 and 1966) on emission and transmission methods. These were just laboratory experiments that made use of the principle of projections; the big breakthrough came in 1964-66 when A.M. Cormack derived the actual mathematical description of reconstruction. He also made good

reconstructions of phantoms using a cobalt source for transmission measurements [9].

The actual construction of a practical CAT device for medical applications began in the late 60's. Hounsfield [20], who was working for the Central Research Laboratories of Electronic Musical Instruments Limited (EMI), completed a head scanner in 1972.

This original device has proved to be so popular that in the short period of time following its introduction, some 1800 such devices produced by 20 different manufacturers have been sold worldwide. The medical importance of CT is confirmed by the award of the 1979 Nobel prize in medicine to A.M. Cormack for his mathematical work and to G.N. Hounsfield for the engineering achievement of building the first scanner.

2.2 MATHEMATICAL PRINCIPLES OF COMPUTED TOMOGRAPHY

This section introduces the terminology and basic derivation of the projection-slice theorem which states that the one-dimensional (1-D) Fourier transform of a projection is a 1-D slice of the 2-D spatial Fourier transform of the function. Mersereau [29] presents a good derivation of the mathematics involved, a portion of which can be found later in this section.

Basically, the reconstruction process is a problem of recovering 2-D signals from their projections. The reconstruction algorithms fall into two categories: one, where theoretically an exact solution can be obtained and the other in which only an approximate solution is possible. Exact methods can be further subdivided into space and frequency approaches. Although the projection-slice theorem can be derived directly in the signal space, it is presently derived in the frequency space for simplicity.

Figure 2 presents the geometry and terminology used throughout this chapter. The variable $f(x,y)$ represents the modifications that the interrogating wave undergoes while travelling in the object. For example, in the case of X-ray tomography, $f(x,y)$ would be the linear attenuation coefficients of various biological tissues; whereas in the case of Ultrasound Computed Tomography (UCT), $f(x,y)$ could represent the velocity profile computed from the Time of Flight (TOF) through the tissue. A ray is a vector normal to the wavefront pointing in the direction of propagation of the wave. In Fig. 2, a few rays are shown equally spaced and parallel to one another. The "value" assumed by the ray is usually the total attenuation of the wave through the object along the path of the ray; in the example shown, this path is a line integral. The angle θ indicates the projection angle; this is the angle the ray paths make with

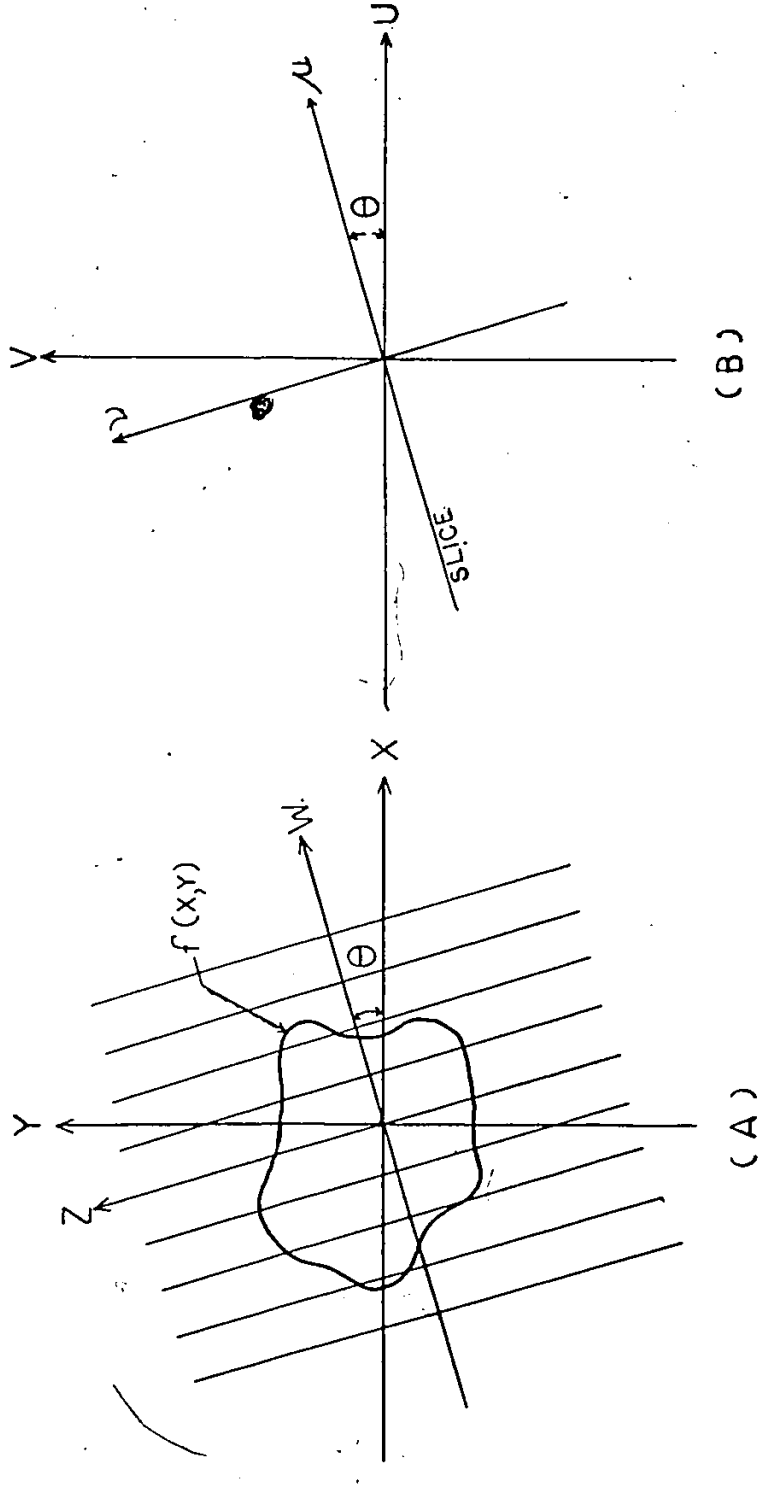

Figure 2: Geometry and Terminology

the y axis. A projection $P_\theta(w)$ is then a set of line integrals of the function f(x,y) taken in the direction of the z axis and is given by the following equation:

$$P_\theta(w) = \int_{-\infty}^{\infty} f(x,y)\ dz \qquad (2.1)$$

The 2-D Fourier transform of the function f(x,y) is given by:

$$F(u,v) = \int\int_{-\infty}^{\infty} f(x,y) \cdot \exp\{-j2\pi(xu+yv)\}\ dxdy \qquad (2.2)$$

A sufficient condition for the existence of F(u,v) is that the function be well-behaved or absolutely integrable. That is,

$$\int\int_{-\infty}^{\infty} |f(x,y)|\ dxdy < \infty \qquad (2.3)$$

The original function can also be obtained from its Fourier transform according to:

$$f(x,y) = \int\int_{-\infty}^{\infty} F(u,v) \cdot \exp\{j2\pi(xu+yv)\}\ dudv \qquad (2.4)$$

A projection $p_\theta(w)$ is a series of line integrals taken along a series of parallel lines normal to an axis which forms an angle θ with the x axis. The relationship between (w,z) and (x,y) is simply one of rotation and is given by the following equations:

$$y = w\cdot\sin(\theta)+z\cdot\cos(\theta) \qquad (2.5)$$

$$x = w\cdot\cos(\theta)-z\cdot\sin(\theta) \qquad (2.6)$$

Therefore, the projection $p_\theta(w)$ can be expressed as:

$$P_\theta(w) = \int_{-\infty}^{\infty} f(w\cos(\theta)-z\sin(\theta),w\sin(\theta)+z\cos(\theta))\,dz \qquad (2.7)$$

The 1-D Fourier transform of a projection is given by:

$$P_\theta(\mu) = \int_{-\infty}^{\infty} f(w\cos(\theta)-z\sin(\theta),w\sin(\theta)+z\cos(\theta))\,dz\cdot\exp\{-j2\pi\mu w\}dw$$
$$= F(\mu\cos\theta,\mu\sin\theta) \qquad (2.8)$$

From Fig. 2, one can see that in the frequency space, (μ,ν) are related to (u,v) as polar coordinates are to rectangular coordinates. Therefore, equation (2.4) can be transformed to the following:

$$f(x,y) = \int_0^{\pi}\int_{-\infty}^{\infty} P_\theta(\mu)\cdot\exp\{j2\pi\mu(x\cos\theta+y\sin\theta)\}|\mu|d\mu d\theta \qquad (2.9)$$

using:

$$u = \mu\cos\theta$$

$$v = \mu\sin\theta \qquad (2.10)$$

The above equation has the significance that if $p_\theta(\mu)$ is known for all values of θ and μ, the original function $f(x,y)$ can be reconstructed exactly. In practice, $p_\theta(\mu)$ is known only at a number of discrete points and in a finite number of directions. By using an algorithm such as the FFT, one obtains samples of the Fourier space along a polar raster as shown in Fig. 3. The use of interpolation is made to convert the known samples on the polar raster into the rectangular raster required for the 2-D inverse Fourier transform. If the sampling is done above the Nyquist rate, then the function $f(x,y)$ can theoretically be reconstructed exactly.

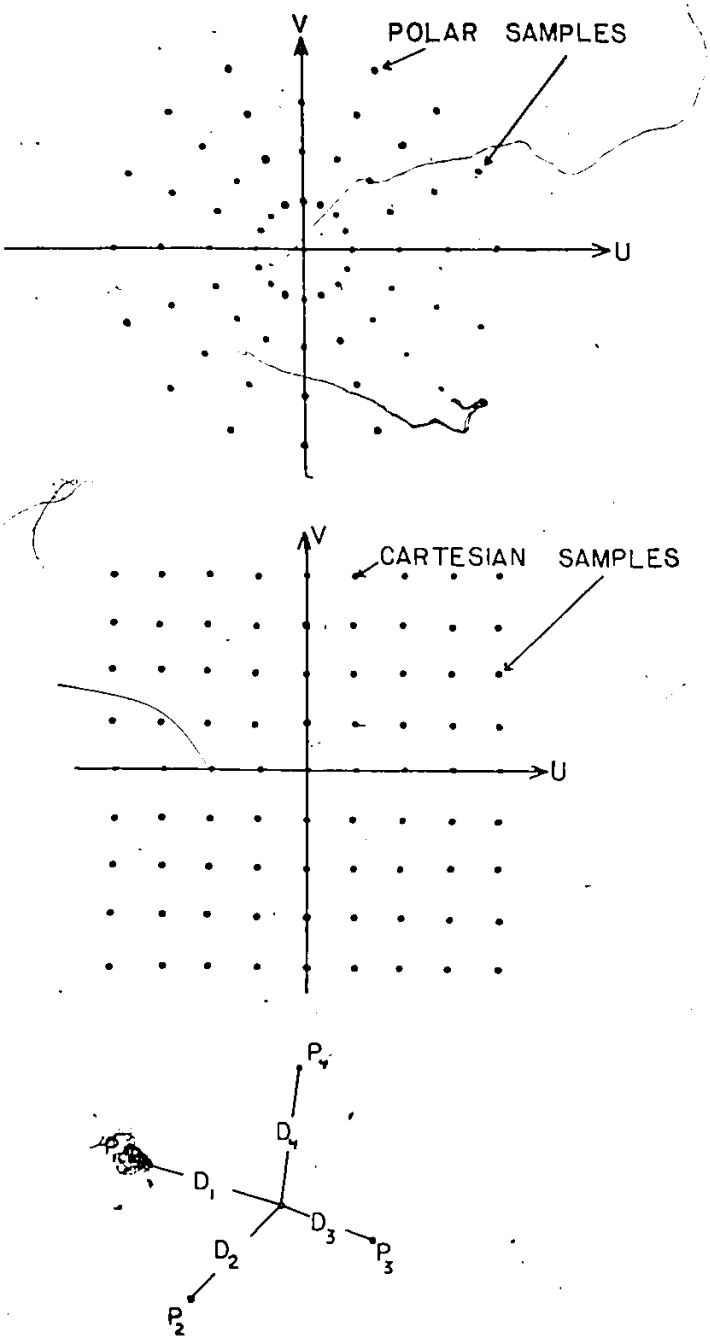

Figure 3: Polar and Rectangular Raster
Linear interpolation as shown above is used to resample the frequency space and convert the sampled grid from polar to rectangular.

2.3 PHYSICAL PRINCIPLES OF COMPUTED TOMOGRAPHY

The previous section introduced the concept of a ray. Also, a projection was defined as the set of line integrals or shadow obtained by the propagation of the "interrogating wave" through the object. In this section, the physical properties of two "interrogating waves" which are used to perform CT are mentionned briefly; namely, X-ray and ultrasound. Since the projection-slice theorem was derived under the assumption of line integrals, the validity of conventional reconstruction algorithms using these techniques is discussed.

2.3.1 X-Ray Tomography

In X-ray tomography, the wave used is a beam of high-energy photons. The parameter that is reconstructed is the linear attenuation coefficient. Since an X-ray beam is non-coherent radiation, phase information is not available. X-ray transmission is presently the imaging technique which comes closest to straight-line propagation. However, a few artifacts are created which alter the final reconstruction.

A collimated X-ray source will produce a parallel beam of photons. Theoretically, this beam should be monoenergetic and have a finite width. Under this assumption, the number of photons at the output (N_o) is related to the number of photons at the input (N_i) by the following equation:

$$N_o = N_i \cdot \exp\left\{ -\int_{-\infty}^{\infty} \mu(x,y)ds \right\} \qquad (2.11)$$

where ds is an element along the path of propagation and $\mu(x,y)$ is the attenuation coefficient at point (x,y).

The above equation is only true for monoenergetic X-rays because in fact, μ is also a function of energy. In practice, the idea of having monoenergetic photons is not valid. It is found that for a constant anode voltage, an X-ray source will give a wide spectrum. Transforming the previous equation to include the dependance of the linear attenuation coefficient on the energy of X-rays will give:

$$N_o = \int_{-\infty}^{\infty} S_i(E) \cdot \exp\{-\int_{\infty}^{\infty} \mu(x,y,E)ds\}\, dE \qquad (2.12)$$

where $S_i(E)$ is the incident photon energy and the attenuation coefficient μ is now a function of energy (E).

In many biological tissues, the linear attenuation decreases with energy. This means a polychromatic source will cause low energy photons to be more absorbed so that the mean of the output spectrum will be higher than the mean of the input spectrum. This is the major artifact caused by X-rays and is called beam hardening.

The other artifact introduced in X-ray tomography is caused by the scattering or diffraction of X-rays at sharp interfaces such as bone/water. Although this effect is small relative to the dimensions of the object, it is nevertheless visible in the final reconstruction. Kak [24] gives a good discussion of the effects of beam hardening on the final X-ray image.

2.3.2 Ultrasound Tomography

In the case of ultrasound tomography, the unknown object is insonified and an attempt is made to determine the acoustic properties of the medium. Because ultrasound is coherent, measurements of both phase and amplitude are possible. Two parameters that are reconstructed are the linear attenuation coefficient and the velocity profile computed from the Time of Flight (TOF) in the medium. Whereas the former parameter was suitable for X-ray CT, it is less than adequate for UCT due to increased reflection, refraction and diffraction effects. These effects indicate types of propagation and consequently losses other than in a straight line.

An ultrasonic wave incident on an interface has a fraction of its energy reflected, another refracted and part of it diffracted depending on the type of interface encountered and the angle of incidence. If the medium

contains only small variations in acoustic impedance, then the wave can be assumed to propagate along a straight line. Standard reconstruction algorithms can then be used and relatively good images are obtained [16], especially in homogenous tissues such as the female breast. Some researchers have gone one step further and applied geometrical optics theory. In such cases, diffraction effects are ignored and ray tracing is performed to find the path of propagation through the object [22];this is done by computing the refractive indices from the velocity profile and applying refraction principles. However, better models are clearly required for the general case of wave propagation in an arbitrarily varying medium which would take all effects into consideration.

One approach to this problem is the one attempted by Mueller et al. [31]. It assumes only small perturbations but includes effects of refraction and diffraction. This is where the first distinction is made between a ray and a wavefront. Previously, only geometrical optics theory had been used to describe wave propagation. The work by Mueller et al. is an attempt at direct wavefront reconstruction which is probably the most suitable to describe acoustic and electromagnetic wave propagation.

2.4 RECONSTRUCTION ALGORITHMS

Reconstruction algorithms are used to obtain the unknown function f(x,y) from its projections. Table 1 gives a list of these algorithms which are performed directly in the signal space. This section describes the two reconstruction algorithms which are the most commonly used [19]. The first one, the filtered back-projection or convolution technique is analogous to the projection-slice theorem but it is performed in the signal space; it gives an exact solution after one iteration. The second one, the algebraic reconstruction technique (ART) is also performed in the signal space but refines an estimate iteratively; this is the algorithm implemented in the original EMI scanner.

TABLE 1

Signal space algorithms

Algebraic Reconstruction Technique	ART
Simultaneous Iterative Rec.	SIRT
Back Projection	BP
Filtered Back Projection	FBP
Matrix Inversion	MI

Figure 4 shows the unknown distribution f(x,y). This function is also shown in sampled form f(i,j) for i,j=1,n.

This implies there are n^2 unknowns one wishes to solve for. Since an nXn reconstruction is desired, a system of n^2 linearly independant equations are required to obtain a unique solution. These equations are obtained from the line integrals evaluated along all the rays within each projection.

The classical approach to solving a set of equations is to write them in a matrix form and solve for the unknown. Refering to Fig. 4, one can write the n^2 equations in a matrix form as follows:

$$P = Q\mu \tag{2.13}$$

The solution of the set of equations, μ, is found by inverting the matrix Q:

$$\mu = Q^{-1}P \tag{2.14}$$

The only problem with this technique is that the size of a typical matrix is so large that the inversion is prohibitively long. For example, if n=100, the matrix Q is of size $10^4 \times 10^4$. This becomes too lengthy for near real time applications. Also, the set of equations obtained is often not well behaved so that the solution obtained may not be correct.

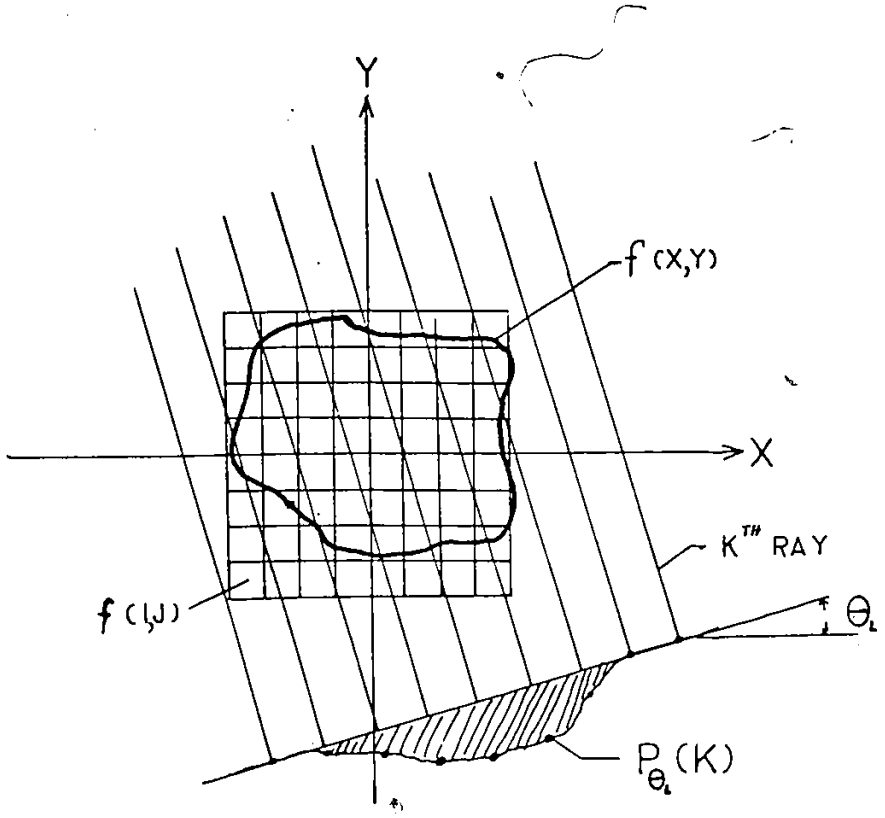

f(x,y)	property of object to be reconstructed
f(i,j)	sampled version of f(x,y) [nXn samples]
k	ray number
l	projection number
Q(i,j,k,l)	weight of pixel (i,j) in ray $P_\theta(k)$
P	projection data in vector form
μ	f(i,j) in vector form [n^2X1 vector]

Figure 4: Terminology

2.4.1 Algebraic Reconstruction Technique (ART)

This reconstruction technique consists in iteratively changing a solution until its projections are consistent with the measured projection data [15]. This is done by first making a guess and refining this guess iteratively until it agrees with the projection data. Usually, the average is used as the initial guess; it is given by the following:

$$\mu_{i,j}^{0} = \frac{\sum_{k} P(k)}{N^2} \qquad i,j = 1,2,\ldots,n \qquad (2.15)$$

where the superscript 0 is the iteration number.

From this initial guess, future iterations can be computed using one of many methods. Two major methods used for the correction factor in ART are additive:

$$\mu_{i,j}^{q+1} = \mu_{i,j}^{q} + \frac{P_{\theta}(k) - P'_{\theta}(k)}{N_{k\theta}} \qquad (2.16)$$

or multiplicative:

$$\mu_{i,j}^{q+1} = \mu_{i,j}^{q} \cdot \frac{P_{\theta}(k)}{P'_{\theta}(k)} \qquad (2.17)$$

where $P_{\theta}(k)$ is the measured projection data and $P'_{\theta}(k)$ is the projection data computed from the solution at the q^{th} iteration.

There are also other variations called partially and fully constrained ART as shcwn below:

$$\text{partially: if } \mu_{i,j}^{q+1} < 0 \text{ then } \mu_{i,j}^{q+1} = 0 \tag{2.18}$$

$$\text{fully: if } \mu_{i,j}^{q+1} > \mu_{max} \text{ then } \mu_{i,j}^{q+1} = \mu_{max} \tag{2.19}$$

where μ_{max} is the maximum known value of the parameter μ.

The SIRT algorithm is basically the same as ART except that the correction is performed on each pixel using the projection data from all projections. A major limitation of ART, SIRT and matrix inversion is that all the data must be acquired before the reconstruction is performed. The sequential nature of these processes make real time applications difficult. However, the ART algorithm is the most suitable to include path alterations due to refraction.

2.4.2 Filtered Back Projection

The simple back projection method is an intuitive approach to the solution of the equations since it is basically the inverse process of data acquisition. The method consists in converting all the 1-D projections into a single 2-D structure. This is done by smearing each projection back onto the unknown along the direction of propagation (the z axis in Fig. 2). The final back projected density at each point has a contribution from each ray passing through it:

$$\hat{f}(x,y) = \int_0^{\pi} p_\theta(x\cos\theta+y\sin\theta)\, d\theta \qquad (2.20)$$

The major artifact created in the reconstruction is that all points are blurred by the "star" shape of the impulse response or point spread function. The effect of the point spread function can be reduced by filtering techniques.

The filtered back projection basically uses the same procedure as in simple back projection except the projections are modified before the back projection is performed [18]. A major type of filtering used is convolutional filtering where the point spread function is reduced or eliminated by convolving each projection with the impulse response of the proper filter. The first step is to rewrite equation (2.9) such that:

$$f(x,y) = \int_0^{\pi} p^*_\theta(x\cos\theta+y\sin\theta)\, d\theta \qquad (2.21)$$

where:

$$P^*_\theta(w) = \int_{-\infty}^{\infty} |\mu| P_\theta(\mu)\cdot\exp\{j2\pi\mu w\}\, d\mu \qquad (2.22)$$

Note that equation (2.21) is similar to equation (2.20); the difference being that p* is back projected rather than p. This implies that a filtering technique must be used to

transform all projections from p to p*. Equation (2.22) can be seen to be the inverse Fourier transform of the function $|\mu|$ multiplied by $P_\theta(\mu)$. However, the convolution theorem states that:

$$a(x) * b(x) = \int_{-\infty}^{\infty} A(\omega) \cdot B(\omega) \cdot \exp\{j2\pi\omega x\}\, d\omega \qquad (2.23)$$

therefore, equation (2.22) can be evaluated directly in the signal space by convolving each projection with another function or kernel. In order to suppress high frequency noise, the coefficients of this kernel are usually taken from a simple boxcar filter at a frequency of 1/2A where A is the distance between adjacent pixels.

2.5 SCANNING CONFIGURATIONS OF CT MACHINES

The advent of high speed digital computers has made possible the physical principles developed 50 years earlier. These dedicated computers control data acquisition, execute the reconstruction algorithm and display the final result.

The ability to sample the interrogating wave at many points along many angles of view of the unknown object is a major requirement of a scanner. The set of samples collected within the same projection are obtained by moving a detector on the side of the object opposite from the source; this motion can be either linear translation or

radial translation of the detector. Successive projections are acquired by the rotation of the source-detector assembly around the object or analogously, by the rotation of the object.

During the past decade these scanners increased in complexity while reducing data acquisition and computation times. The reduction of data acquisition time is an important factor in a commercial scanner since long scan times introduce artifacts due to the motion of the patient. The reduction of computation time is also important so that the radiologist can judge the quality of the image while the patient is waiting. Figure 5 shows a few scanning configurations. They can be classified into three major generations of machines.

Figure 5-a gives an example of a first generation scanner. These are single-source—single-detector scanners. The scanning is performed by moving the source and the detector simultaneously in the transmission and receiving planes. The detector is sampled at specific locations so that the ray paths consist of equally spaced parallel lines. The source-detector assembly is then rotated and the procedure repeated for the subsequent projections. The original EMI scanner was of this generation; it required 4-5 min. of data acquisition time with 30 s additional

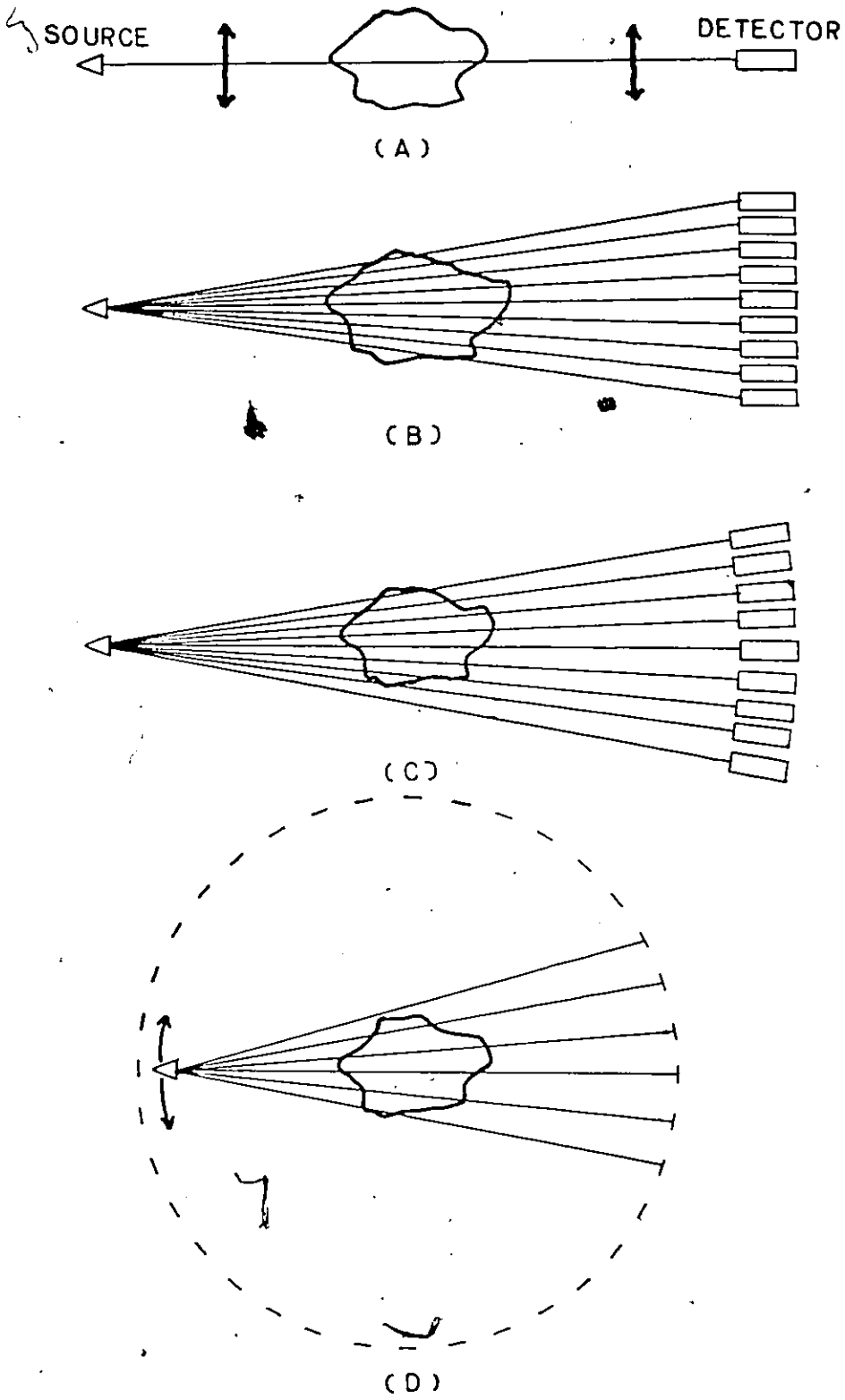

Figure 5: Four Scanning Configurations

processing time. The final reconstruction contained artifacts due to motion during scanning; nevertheless, it demonstrated the dramatic increase in contrast obtainable using this technique.

Second generation scanners are of the single-source—multi-detector type. Figure 5-b,c and d show three such implementations. These configurations are the first to make use of fan beams in order to eliminate the requirement of many sources. Figure 5-b represents the case where the detector array is placed in a line. Each detector is then sampled to give the required translation effect without actually having any moving parts. Figure 5-c is essentially the same except the detectors are placed in a circular configuration. The number of detectors again ranges from 20 to 60. Finally, Fig. 5-d eliminates motion of the detectors completely. In this case, approximately 500-600 detectors are placed in a circle. Only the source is rotated and the proper detectors are sampled. Data acquisition times are then reduced to the order of 4-5 s. The price of scanners is higher however due to the number of detectors.

Third generation machines are of the multi-source—multi-detector type [14]. The unit being built at the Mayo Clinic, called the Dynamic Spatial

Reconstructor (DSR), has as objective real-time imaging of the heart. This requires 240 slices of 127x127 pixels at a rate of 60 frames per second which implies acquisition and computation rates of $60x240x127x127 \approx 2.3x10^6$ pixels/s. The resulting images have high temporal resolution as well as high spatial resolution in the three dimensions of the object under study.

Chapter III

REVIEW OF MICROWAVE IMAGING TECHNIQUES

Microwave imaging is a technique consisting in the use of microwaves as the interrogating wave to find the shape, location and composition (electromagnetic properties ε and μ) of an unknown object. Both reflected and transmitted waves (backward and forward scattering) can be utilized. MCT can be considered to be a special case of microwave imaging where a slice of the object is reconstructed. Earlier development of computed tomography has so far been directed towards the improvement of resolution and the decrease in reconstruction times. Tomographic techniques using X-rays and ultrasound have been studied greatly in the past and many advanced machines are available commercially. However, in certain applications, X-ray and ultrasound imaging have limited capabilities. For example, X-ray tomograms of the lungs provide low contrast while ultrasound tomograms suffer from high attenuation in the lung tissue. In addition, the use of X-rays occasionaly necessitates the injection of contrast materials or tracers.

In this chapter, microwaves are compared with other interrogating waves and the possibility of their use to

reconstruct an object from the transmission data is investigated. Also, a review of previous work on inverse scattering is presented, followed by a discussion of the requirements of an instrument to investigate microwave computed tomography.

3.1 MICROWAVES AS AN INTERROGATING WAVE

Although there is a large body of literature dealing with the "forward" scattering problem [12],[25],[26], a relatively smaller number of attempts have been made to solve the "inverse" scattering problem of reconstructing the dielectric properties of an irradiated object from the knowledge of the scattered field measured at discrete points [21],[30].

Perhaps one reason for the limited amount of research in the area of inverse scattering is the complexity introduced by the increased contribution of the diffracted field to the total field. The electric field at all points must satisfy the wave equation:

$$(\nabla^2 + \kappa^2) \cdot E_z(x,y) = 0 \qquad (3.1)$$

where:

$$\nabla^2 = \frac{\partial^2}{\partial x^2} + \frac{\partial^2}{\partial y^2} \quad , \quad \kappa = 2\pi/\lambda = \omega\sqrt{\mu\varepsilon} \qquad (3.2)$$

The total field is the sum of the incident field and the scattered field:

$$E_T = E_i + E_s \tag{3.3}$$

where E_i is the incident field and E_s is the scattered field.

Diffraction is a phenomenon that occurs when the wavelength of the incident wave is of the same order of magnitude as the dimensions of the scatterer. Table 2 gives a comparison of the wavelengths in air for the three imaging techniques.

TABLE 2

Wavelength in air for the three modalities

modality	frequency	wavelength
X-ray	av 17.4×10^{18} Hz	0.172 A
Ultrasound	5 MHz	0.007 cm
Microwave	10 GHz	3 cm

In the case of X-rays, the wavelength is many orders of magnitude smaller than the dimensions of the details of the irradiated objects and the energy propagates along straight

lines (rays). Therefore, because of its similarity to light propagation, X-ray projections are sometimes called shadows. The wavelength in air of 10-GHz microwave radiation is the longest of the three and is therefore the longest compared to the dimensions of the irradiated object. This implies that diffraction effects may be expected to predominate over other types of propagation. The complexity of the problem is then increased since the diffraction effects cannot be derived using the special case of geometrical optics theory. Also, if a wavefront several wavelengths wide is needed, the use of microwaves necessitates larger apparatus.

Tables 3 and 4 give a comparison of the wavelength and attenuation of 5-MHz ultrasound along with microwaves (3 and 10 GHz) in various materials. An important observation that can be made from these tables is the fact that ultrasound is attenuated greatly in air while propagating easily in water. The inverse holds for microwaves; they are are not attenuated in air and undergo a 30-dB/cm attenuation in water.

Also, from Table 3, the difference in wavelength between microwaves and ultrasound introduce a comparable loss of resolution in the scatterer. Microwaves (10-GHz) have wavelengths approximately 15-20 times longer than 5-MHz ultrasound and hence a comparable loss of resolution might be expected in the final reconstruction. Microwave imaging

TABLE 3

Wavelength (cm) in a few materials

Material	5MHz Ultrasound	Microwave 3 GHz	Microwave 10GHz
air (STP)	0.0066	10.0	3.0
bone	0.066	3.5	1.4
fat	0.029	4.2	1.4
muscle	0.032	1.4	0.47
polyethylene	0.04	2.0	2.0
skin	0.031	1.5	0.47
water (30°C)	0.031	1.1	0.47

TABLE 4

Attenuation (dB/cm) in various materials

Material	5MHz Ultrasound	Microwave 3 GHz	Microwave 10GHz
air (STP)	60.0	0.0	0.0
bone	10.6	1.118	2.8
fat	3.5	1.032	2.2
muscle	7.0-14.0	5.341	30.0
polyethylene	24.0	0.0007	0.0007
skin	-	5.691	23.0
water (30°C)	0.011	2.75	30.0

may however improve the contrast in some objects, especially in biological tissues. For example, the linear attenuation constant of 60 keV X-rays in biological tissues varies roughly between 0.19 for fat and 0.222 for red blood cells

(Data taken from Zaklad [35]). On the other hand, for 10-GHz microwaves, the corresponding linear attenuation constants are 0.6 for fat and 0.001 for blood cells (Data taken from Johnson and Guy [23]).

Electromagnetic radiation of wavelength near 1 cm reduces resolution, while enhancing contrast, so that they may provide a good trade-off between the two. Also, microwaves are similar to ultrasound in that coherent sources are available; hence, both amplitude and phase information can be retrieved. The possibility of recording a complete phase and amplitude hologram[1] may yield more information about the scatterer. However, a relatively complex signal processing system is required for the reconstruction.

Since little is known about MCT, there is a need to further investigate this area of science. Image reconstruction using a wave in the microwave part of the spectrum is a new concept; it is therefore worthwhile to study the propagation characteristics in an object of arbitrary composition.

---

[1]A hologram is a record of the amplitude and/or phase distribution measured in the observation plane.

3.2 EARLIER MICROWAVE IMAGING TECHNIQUES

Earlier work using microwave imaging techniques has been directed mostly towards scattering from metal objects, the detection of buried structures and recently, medical imaging [25],[1],[27].

Scattering from metal objects is a problem arising in many areas. One of these applications which is of military interest is an area of continuing research; that of target shape estimation using radar. This type of signal analysis involves reflection measurements at very large distances [4]. On the other hand, several researchers have been involved with the forward scattering problems where transmission information is used. In the mid 50's King [25], Kodis [26] and Row [32] studied forward scattering from metal obstacles of simple geometrical shapes. The inverse problem arises when the scattered field is known at specific points and an attempt is made to determine the shape and position of the scatterer. Imbraille and Mittra [21] examined the problem of 2-D inverse scattering. They used an iterative technique to estimate the points of zero electric field representing the boundary of the metal obstacle. After computing a number of these points of zero total field intensity, they plotted the results and compared them to the original structure. This technique is relatively lengthy and laborious in order to get a good

estimate of the shape of the object. Also, it can only be used to solve for scattering from objects with simple boundary conditions such as metal surfaces.

Detection of buried objects is another area which received some attention in the past. Anderson [1] used microwave holography to detect dielectric as well as metal scatterers concealed in low-loss media. In this case, the direction of propagation of the interrogating wave is perpendicular to the plane of reconstruction. Both phase and amplitude are measured in the observation plane and the image is "focused back" in the object plane. Lytle [28] attempted to locate buried mine shafts. This was done by lowering the microwave source in one borehole, the detector in another and using the cross-borehole transmission data to reconstruct the medium between the two which is known to contain the tunnel. By selecting the proper frequency and with the use of ART, fairly accurate cross-sections of the tunnel were obtained. This reconstruction algorithm neglects diffraction effects and assumes straight line propagation; hence, the final reconstruction clearly showed the diffracted field around the edges of the tunnel.

Applications oriented towards medicine have been few and slow in coming. It is only recently that interest has been kindled in this area. Greg et al. [17] have used ART to

reconstruct an object from 10-GHz microwave transmission data. The object was matched to the surrounding medium by inserting it in oil. The best resolution obtained at this frequency is about 1 cm. They attempt the reconstruction of two separate lucite rods 1.6 cm in diameter and separated by 7.3 cm. The scattering from the lucite rods is clearly visible in the final reconstructions.

Larsen and Jacobi [27] are the first to perform microwave imaging of an organ. They obtain the spatial distribution of microwaves transmitted through a canine kidney. The kidney is immersed in water to match the surrounding medium to the object. The object is then irradiated with 4-GHz microwaves and the attenuation and phase shift are measured on the opposite side (this gives one projection only). Plots of both these parameters show the general structure of the kidney, but they contain many artifacts due to diffraction.

In all these attempts, there is one common factor; the object dimensions are comparable to the wavelength and hence the total field contains large contributions due to diffraction. Rather than ignore diffraction effects, perhaps it may be possible to interpret diffraction as valuable information about the object and incorporate this in the reconstruction algorithm. Hence, there is a need for

an instrument to systematically study the characteristics of electromagnetic waves scattered from objects of arbitrary composition. This instrument would have a chamber in which various objects can be inserted in order to measure the perturbance of the electric field that they create. The next section presents the requirements of such an instrument.

3.3 DESIGN CRITERIA OF A MICROWAVE IMAGING INSTRUMENT

Since the instrument is to be used to study scattering from arbitrary objects, it is advantageous to simplify the geometry of the problem. This can be done by performing the measurements in a controlled environment such as a parallel-plate chamber. The idea of using a parallel-plate configuration is basically to make objects placed inside appear electrically as infinitely long, uniform cylinders [25]. In this way, 3-D scattering problems are reduced to 2 dimensions. Furthermore, to insure propagation in the TEM mode only, which results in a simplification in wavefront analysis, the plate separation must be less than 1/2 of the shortest wavelength.

Another desired characteristic of the instrument is that the incident wave be uniform and plane. These constraints placed on the source facilitate the calculations since the amplitude and phase of the wave are equal along a plane perpendicular to the direction of propagation.

The minimization of the internal reflections from the walls of the chamber and the detector is another consideration. In other words, the field measured at the detector should have its main contribution due to scattering from the object and contain minimal contributions introduced by the reflections from the walls.

If all the above conditions are satisfied the problem reduces to that of a uniform plane wave incident upon the object and the field measured in the observation plane has components only due to the 2-D scattering from the object. The next chapter introduces the actual design procedure and the final chamber characteristics that meet these design criteria.

Chapter IV

EXPERIMENTAL APPARATUS

In this chapter, a description of the MCT-I system designed to study microwave computed tomography (MCT) is presented. This name was chosen simply because it is the first version of an instrument to be used to study microwave computed tomography.

The first section gives the overall objective of such an instrument followed by sections describing respectively the system hardware and software.

4.1 OBJECTIVE OF THE MCT-I SYSTEM

The overall objective of the MCT-I system is to enable the user to study the feasability of using microwaves to reconstruct the spatial distribution of the dielectric properties of an unknown object. Eventually, it is hoped that the more general three dimensional problem can be solved by using principles derived from the simpler two-dimensional case.

The MCT-I system requires a source of microwave radiation as well as a chamber or waveguide for them to propagate in and a detector to measure the electric field intensity. The source and detector must be able to, respectively, radiate and measure the field without disturbing it in any way. The amplitude of the electric field is measured behind the object for a number of different directions or projections. This is accomplished by moving the source and detector along prescribed trajectories under computer control. Since the instrument is a research tool rather than a commercial device, speed optimization is of no concern. Therefore, the implementation of simple scanning configurations and data acquisition techniques are the immediate objectives of the system. The transmission data, be it amplitude, phase, or both, is then stored on a disk for future processing.

The characteristics mentionned above are the basic requirements of the MCT-I system. It enables the operator to quickly determine the scattered field from arbitrary objects. The following section will present the design procedure and final specifications of the system hardware.

4.2 MCT-I SYSTEM HARDWARE

The scanner is basically a single-source single-detector device as described in first generation X-ray machines. All operations of the scanner are controlled or performed by a

PDP11/34 multi-user minicomputer running on RSX-11M. The PDP11/34 has three RL01 disk drives giving it a total storage capacity of 15 Mbytes.

Figure 6 shows the MCT-I system in block diagram form. The system contains two major sections: a microwave section where the experiment itself is performed and a digital section which controls the apparatus using a PDP11. The microwave section is composed of an oscillator which produces the incident plane wave, a parallel-plate region where the object is inserted and a detector to measure the resulting field distribution.

The digital section is used to control and monitor the mechanical motions of the scanner as well as perform the calculations required by the experiment. The PDP11 can position the object and the detector by driving two separate stepper motors. It also controls data acquisition using the K-series peripherals (A/D converter and digital I/O) as well as display the resulting data. The next three subsections will describe, respectively, the chamber, the microwave circuit and the digital instrumentation of the MCT-I system.

4.2.1 Chamber Description

There were two basic approaches used in the design of the parallel-plate chamber. The original configuration had a

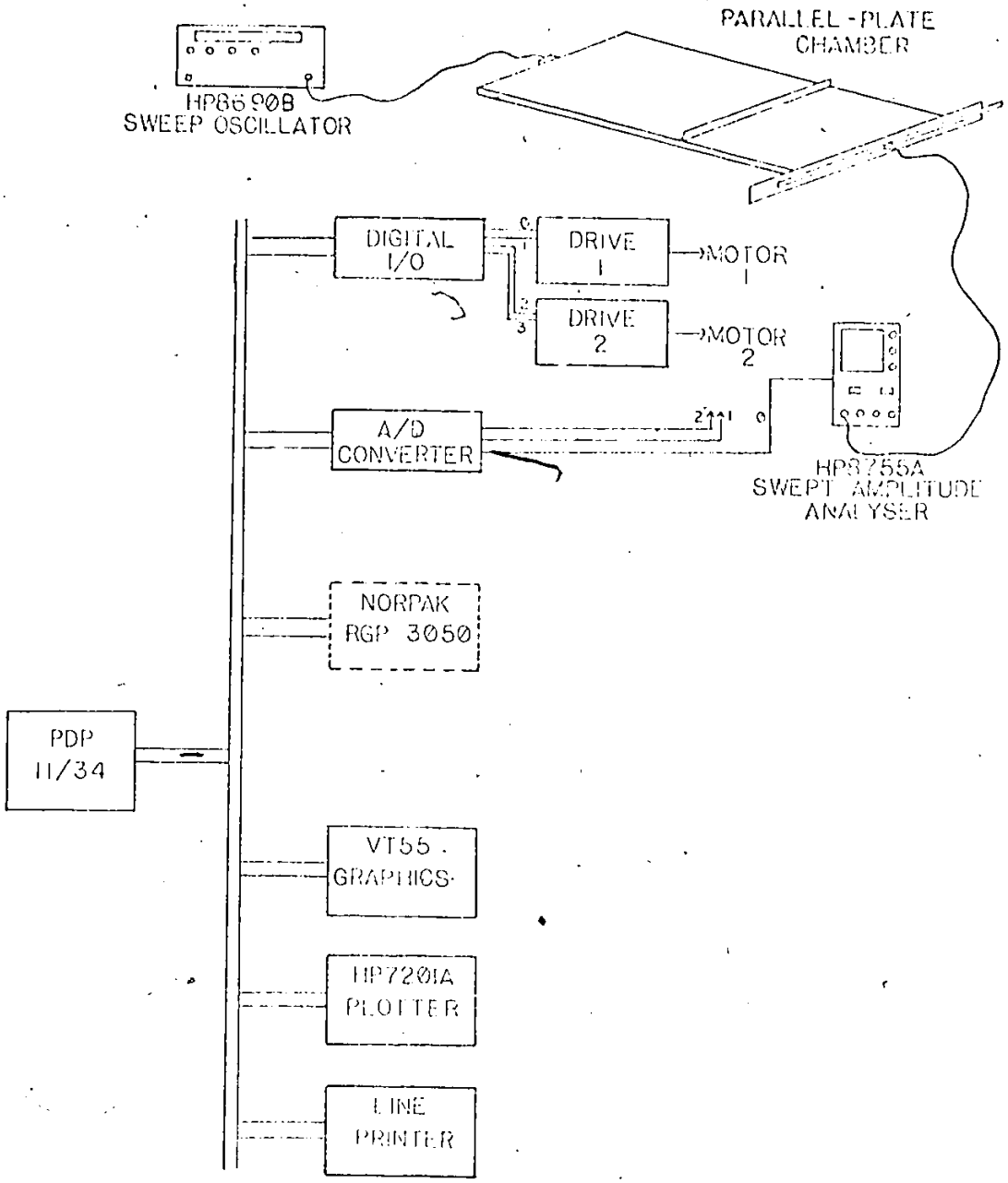

Figure 6: Hardware Block Diagram of System

circular slot cut in the top plate through which a dipole was inserted and was used as a detector antenna. The reason being that the distance between the detector and the phase center of the source remained constant at 1 m throughout the scanning procedure, thus simplifying phase computations. However, errors due to mechanical vibrations and vertical motion of the dipole in the slot turned out to be too great. These detector positioning innacuracies forced the adoption of a configuration using linear translation at the end of the plates.

Figure 7 shows the external dimensions of the parallel-plate chamber incorporated in the MCT-I system. Like the name implies, the chamber consists of two metal plates parallel to one another. In this case, the 61 cm (2') x 122 cm (4') x 0.159 cm (1/16") thick plates are made of brass and aluminum for the top and bottom plates respectively. The 1.27 cm (1/2") separation between the plates is chosen for electrical and mechanical considerations. First, operation around 10 GHz in the TEM mode only is desired. This implies a plate separation of at most a half of a wavelength which equals 1.5 cm at 10-GHz. The dimension available in stock in stores which is smaller than half of a wavelength is 1.27 cm (1/2").

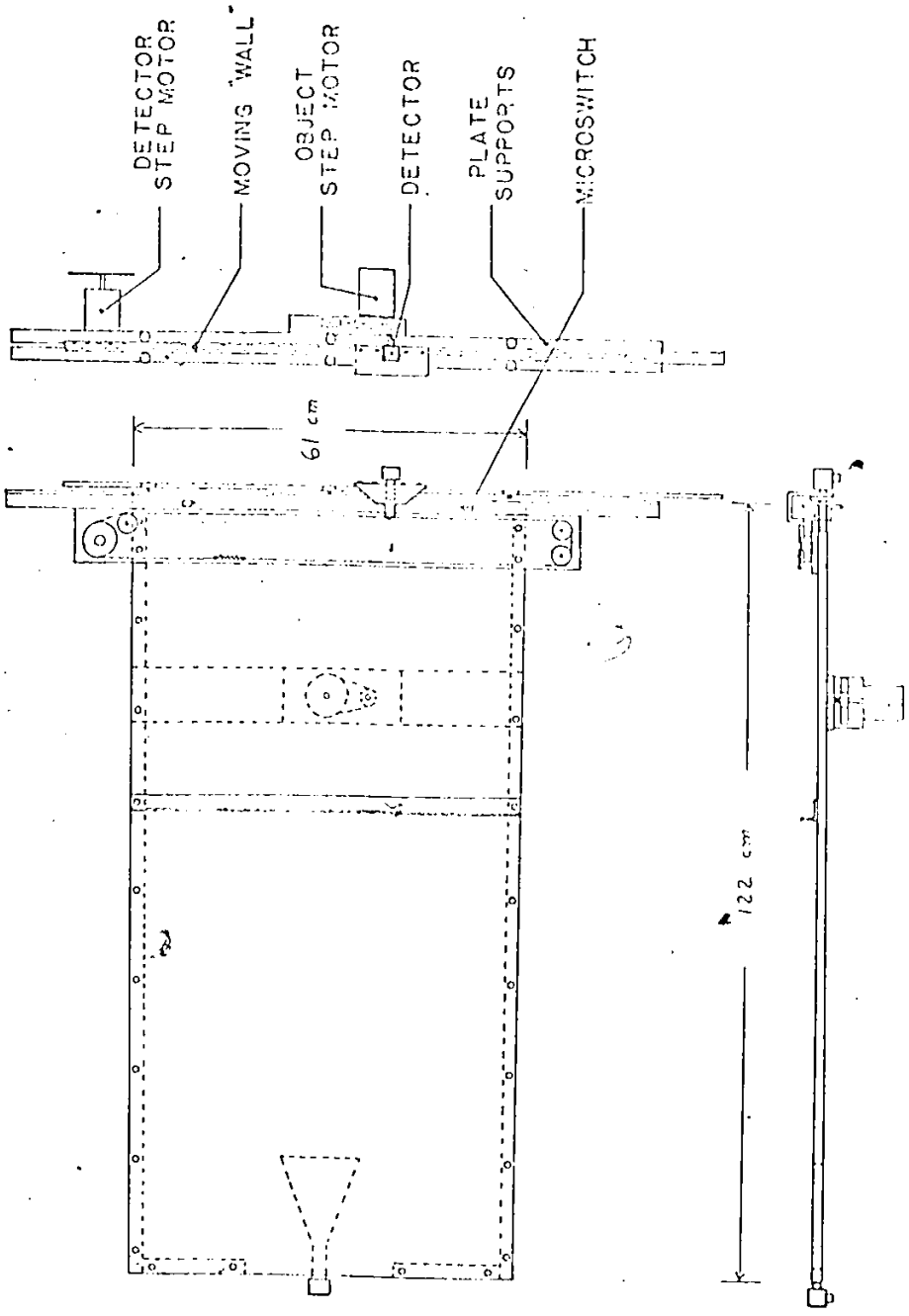

Figure 7: Parallel Plate Chamber (External)

The external dimensions of the plates are 61 cm by 122 cm; or in terms of wavelengths, 20 by 40 . Ideally, the dimensions should be infinite so that the effects of reflections from the walls are minimal. Although the plates King used in his experiments are approximately twice this area, 7442 cm^2 (8 ft^2) is of sufficient size for initial measurements as will be seen in chapter 5 where the results are presented. The analytical problem of taking accurate account of the finite plate dimensions is prohibitively difficult. Instead, the effect of edge reflections is made negligible with the addition of absorbing material along the inside perimeter of the chamber.

Figure 8 shows the internal configuration of the absorbing material within the chamber. There are two materials along the periphery of the chamber; namely, aluminum bars that provide the required 1.27 cm separation of the plates and absorbing material glued alongside it to limit internal reflections from the walls. In this way, the plates electrically appear to be of infinite dimensions although they are only 7442 cm^2. This absorbing material is placed around the chamber in two layers. The first layer is simply of rectangular cross-section and is placed alongside the metal separators. The second layer, or innermost layer is composed of small tapered triangles to further reduce internal reflections.

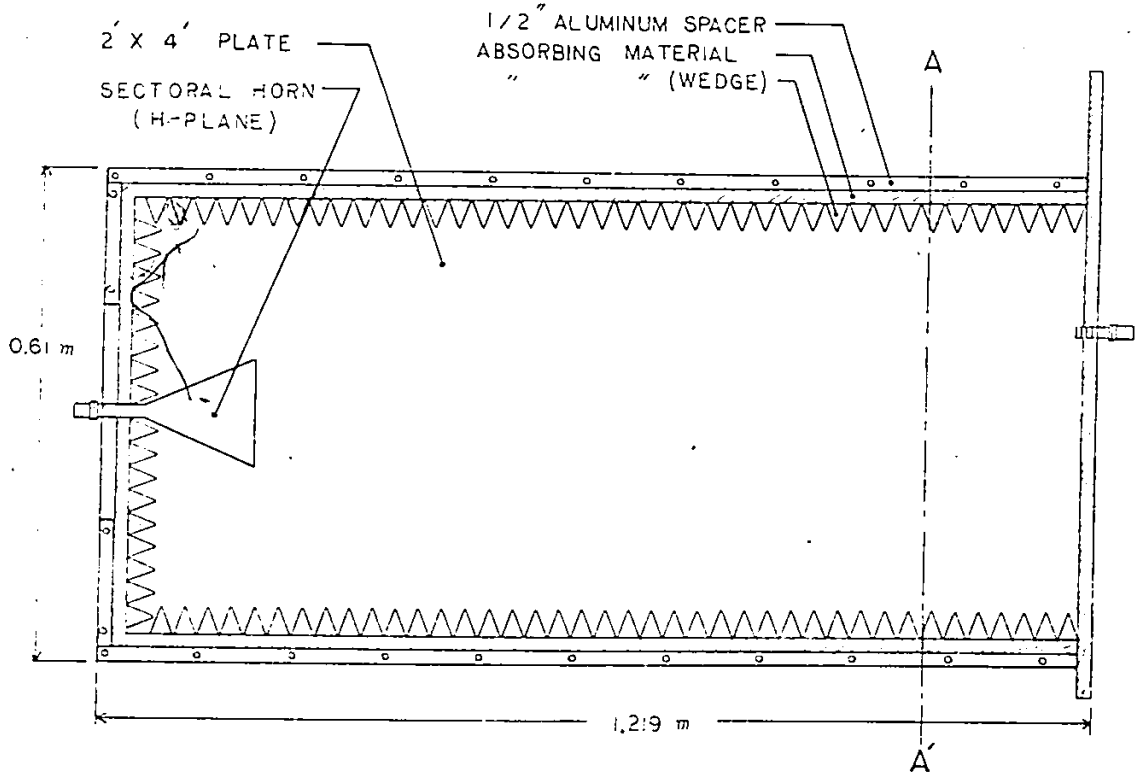

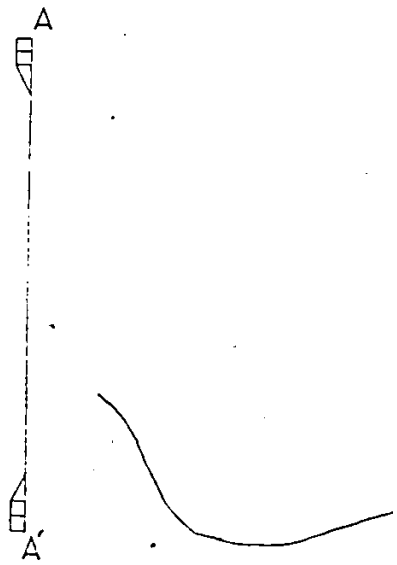

Figure 8: Parallel Plate Chamber (Internal)

The distance between the source and the obstacle within the plates can be varied but is generally of the order of 30 wavelengths. At this distance, the amplitude of the incident wave is essentially constant over the width of most obstacles inserted. Therefore, the assumption of a plane wave incident on the obstacle is a relatively good one.

From the diagram of the chamber, one can also observe that the scanning geometry used is linear translation. This can be seen by observing that the detector is mounted on a sliding aluminum bar at the end of the plates. The detector protrudes within the plates by passing through the absorbing material and is therefore the only metal part inside the chamber except for the sectoral horn at the source end. This entire assembly, which also includes a piece of rectangular absorbing material, therefore appears as a "matched wall" at the back of the chamber. This matched wall can move along 2 sets of pulleys so that the detector can sample the electric field at various points along the observation plane without disturbing it.

With all these precautions, the field measured at the back of the chamber is still not that of a plane wave. It includes the remaining effects of internal reflections within the chamber as well as the non-uniform radiation pattern of the horn. In order to take these effects into

consideration, a calibration procedure is performed. This consists of measuring the empty-chamber scattering characteristics and subtracting it from the field observed with the object inserted in the plates.

4.2.2 Microwave Circuit

In the previous section, the parallel-plate chamber was described in detail; it is now introduced as an element within a microwave circuit. A description of the individual components of this microwave circuit is also presented.

The microwave components contained in the MCT-I system are shown in block diagram form in Fig. 9. An HP8690B sweep oscillator is used to provide the source of 10-GHz electromagnetic radiation. This is squarewave modulated with a 27.8 KHz signal from the amplitude analyser and fed to a directional coupler. The directional coupler is connected to a sectoral horn which radiates a plane TEM wave in the chamber; it is also used to get part of the input signal as a reference for the HP8755A swept amplitude analyser. The signal is then detected with an HP11664A crystal detector.

In practice, it is difficult to obtain a perfectly plane wave of radiation from a source. The design for the chamber of the MCT-I system was that it be relatively plane within

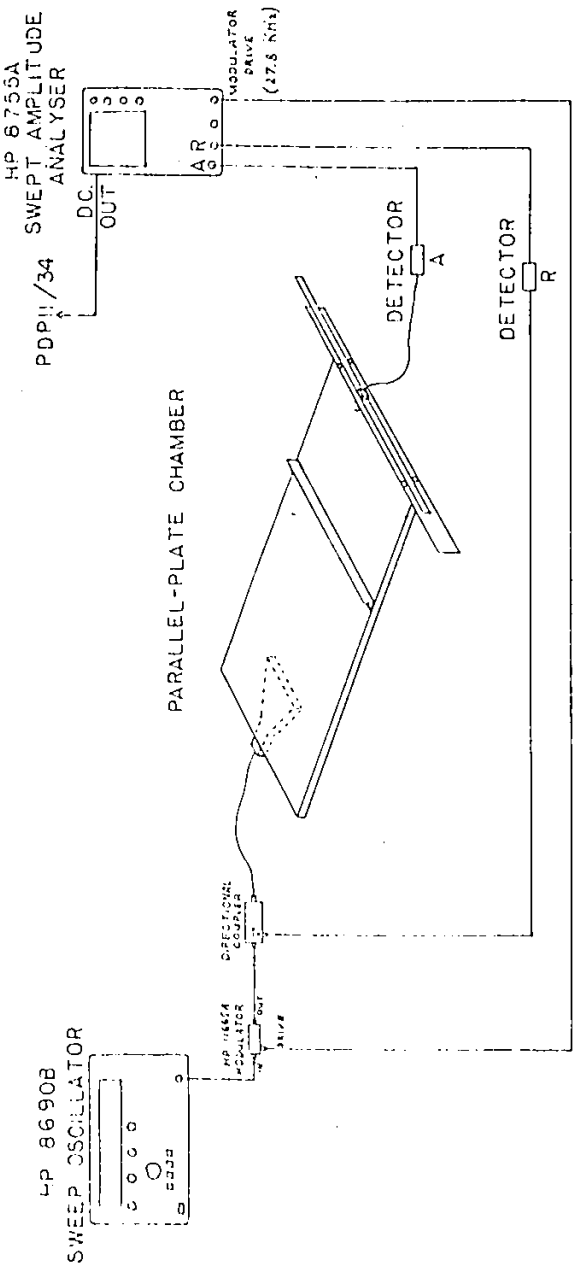

Figure 9: Microwave Circuit used in Scanner

the angle subtended by the object. The first measurements were done with an open-ended waveguide and this condition was obeyed, but it had only a small gain, thus warranting the design of a sectoral horn. In addition, since the open-ended waveguide had a relatively large beam width, the incidence angle onto the walls of the chamber was large, thereby increasing the internal reflections. The sectoral horn is designed so that the radiated energy is directed mostly toward the object, and hence stray radiation on the walls of the chamber are reduced. The horn is flared in the H-plane and so is called an H-plane sectoral horn[2]. The aperture of the horn is 1.25 cm x 14 cm (0.423 x 4.66 in terms of 3 cm free space wavelengths). With these dimensions, a gain of 9.5 dB is obtained and the corresponding half-power beam width is 16°, which is the angle of detector motion at the end of the chamber.

The approach used in the design of the detector is a bit more complex. The idea is to measure the electromagnetic field in the chamber without disturbing or altering it. Figure 11 shows a tree structure of the various detectors that were tried. Initially, the top plate had a slot cut in it where a detector was inserted. This detector was mounted on an arm pivoting about the phase center of the source.

---

[2]The gain and beam width are taken from: J.D. Kraus, "Antennas", McGraw-Hill Book Co., N.Y., 1950, pp.371.-381.

Both an electric dipole and a magnetic loop antenna were tried. In the two cases, variations of up to 3 dB in attenuation were due to vertical motion of the antenna within the plates. The present MCT-I system uses linear translation at the end of the plates. Linear translation is adopted because mechanical positioning innacuracies can be made smaller at the end of the plates. The antenna presently used is a dielectric filled waveguide with quarter wavelength chokes on each surface providing electrical contact with the plates. This waveguide is inserted through an aluminum sliding wall at the end of the plates. The aluminum bar has some absorbing material glued on its inside surface so that the only metal inside the chamber is the aperture of the waveguide. This antenna is connected to a detector of the swept amplitude analyser.

The swept amplitude analyser measures the ratio of the detected signal to the reference signal at the horn. This ratio gives a measure of the transmission loss in dB's between the source and the detector. The PDP11 can read this attenuation by sampling channel 0 of an A/D converter which is connected to a DC signal proportional to the power ratio. The empty plate characteristics obtained using this detector are included in the next chapter on results.

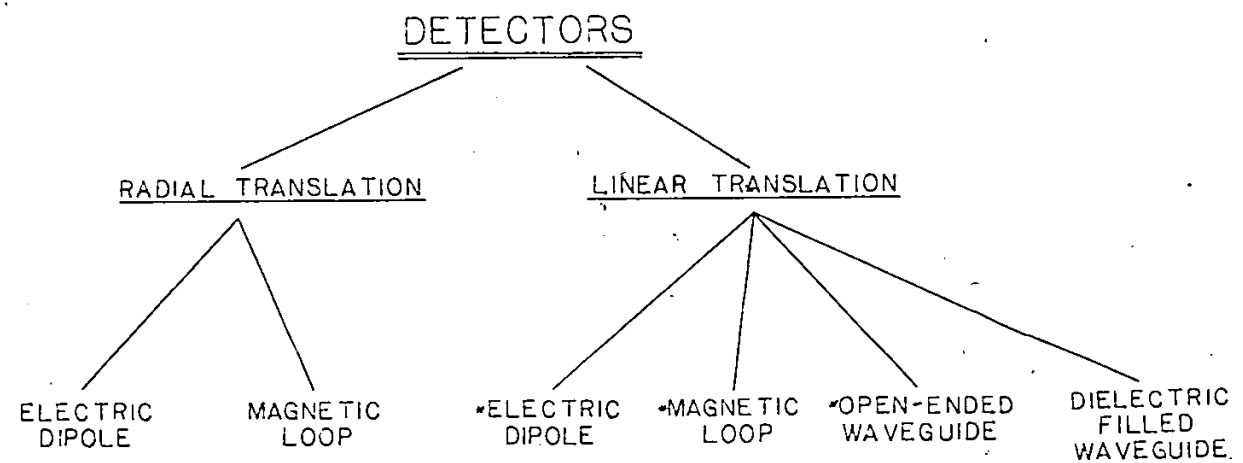

Figure 11: Tree structure of detectors tried

The measurement error introduced by the A/D converter is minimized by averaging. The PDP11 performs 5 consecutive A/D conversions while allowing proper settling time between them; the measured value is then taken to be the average of these readings. Since most experiments are performed using a 5-dB per division setting, the quantization error introduced is 1/40 dB's and can therefore be neglected for the purpose of this project.

The circuit described above is therefore used to generate the interrogating wave, irradiate the object to be studied and finally, measure the amplitude of the scattered electric field at specific locations behind the object. The next subsection describes how a PDP11 is used to control the apparatus.

4.2.3 Digital Instrumentation Circuit

In order to automate the MCT-I system, the PDP11 must control linear translation of the detector and rotation of the object. This interface is accomplished using the K-series laboratory peripherals. The A/D converter (model AD11-K) is a 12-bit-successive-approximation converter with 16 channels having input voltage ranges of ±5 Volts and settling time of 20 μsec. The digital I/O (model DR11-K) is a general purpose device for transfer of up to 16 bits of data in parallel.

The actual interface between the PDP11 and the experiment is therefore in the form of a digital signal to motion transduction. This is accomplished with the use of two Superior Electric Slo-Syn step motors (model M092-PC09). The torque requirements of these motors are computed from the mechanical driving requirements of the detector and the object. In this case, both motors are rated at 1.412 N•m (200oz-in) torque and 1.8°/step. The motors are actually controlled by STM-103 translators to simplify the electrical driving requirements; these being 5 V pulses, 30 μsec long. These TTL-level pulses are provided by the 4 LSB of the digital I/O. Bits 0 and 1 are used respectively for the clockwise and counterclockwise motion of the detector motor while bits 2 and 3 are for object rotation in the same directions.

The driving mechanism used for the detector is shown in Fig. 12. Each 1.8° step the motor makes is translated into 400 μm of linear displacement of the detector. There are 962 steps possible between the two microswitches at either end of the detector drive thus allowing user-definable resolution within each projection. The microswiches are connected to channels 1 and 2 of the A/D converter and are sampled after each step to provide position feedback to the PDP11. They also prevent damage of the detector drive by disabling the motor when the detector position exceeds these

limits. Although accurate positioning encoders would be ideal, these two microswitches can be used to repeat an entire projection if the number of steps taken between them is not correct.

The object drive used in the MCT-I system is much simpler. The object is driven by the second stepper motor using a synchronous belt drive with 2 gears. The gear ratio is 4:1 so that a 1.8° motor step is translated into a 0.45° angle of rotation of the object. This allows a possible 800 projections over a complete revolution of the object; the operator can therefore select the desired number of projections by double or triple stepping the motor. There are presently no position detection devices on the object drive, but they can be easily added if the need arises. Figure 13 shows the object drive mechanism. The objects are attached to the shaft of the larger gear with a section protruding through the bottom plate.

The remaining components in the digital instrumentation section include various display devices that can be used to show the collected data or final reconstructions. These include a VT55 graphics terminal, an X-Y plotter and eventually, a graphic display. Presently, the VT55 is used for immediate results since it is on a 9600 baud line whereas the X-Y plotter is at 600 baud which is much slower.

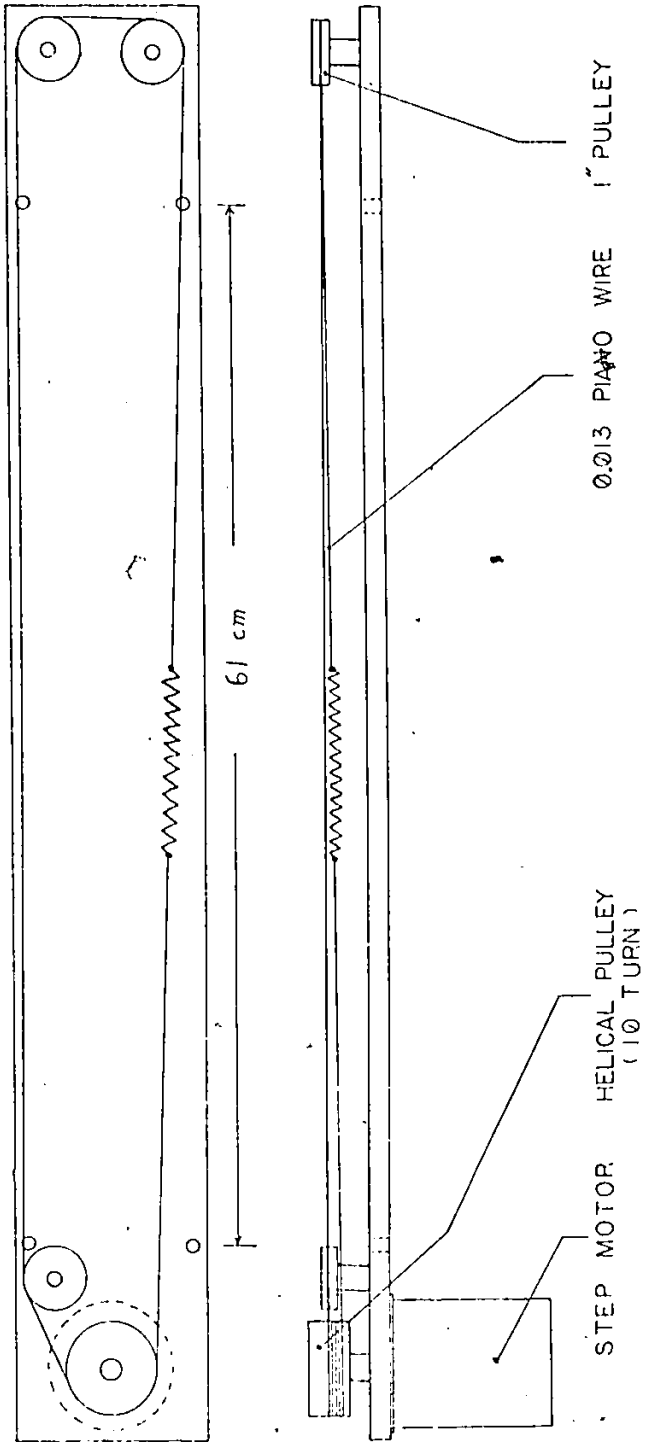

Figure 12: Detector drive

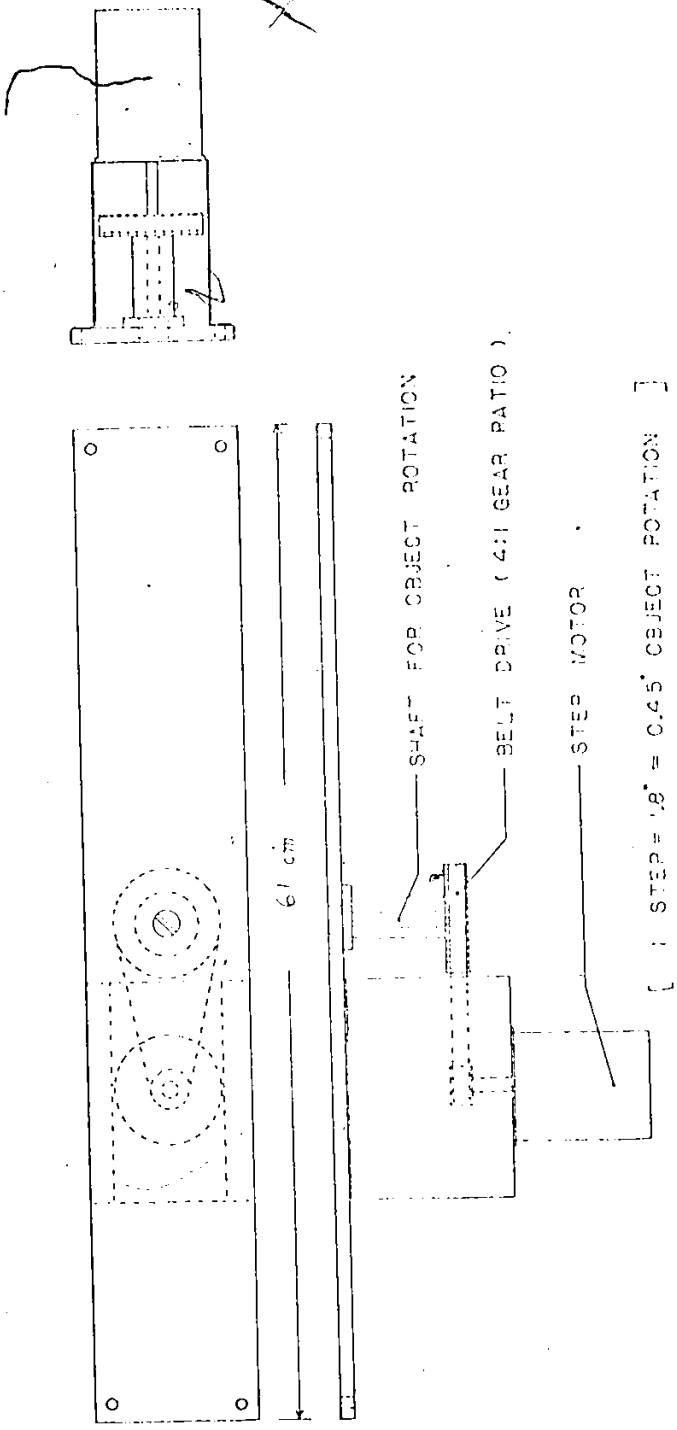

Figure 13: Object drive mechanism.

4.3 MCT-I SYSTEM SOFTWARE

This section presents the software developed for the MCT-I system; this includes data acquisition, storage and display programs for various devices.

The data acquisition itself is relatively simple; it consists in reading channel 0 of the A/D converter. The data acquisition program (ACQUIRE.FTN) averages the readings and checks the microswitches for correct displacement of the detector. This is done by reading channels 1 and 2 of the A/D converter regularly; the voltage read indicates whether the corresponding microswitch is on or off.

Figure 14 shows a flow chart of the data acquisition program. As mentionned earlier in the hardware section, the detector drive has 962 motor steps between microswitches. However, the user may want only 100 samples within a projection so that a user step would equal approximately 9 motor steps in this case. This implies the operator must specify how many user steps and how many projections he wishes to do on a particular scan. The program ACQUIRE.FTN then computes the corresponding number of motor steps per user step for both detector motion and object rotation. From these variables, the actual scan is performed until all projections are stored on disk and the data file is closed.

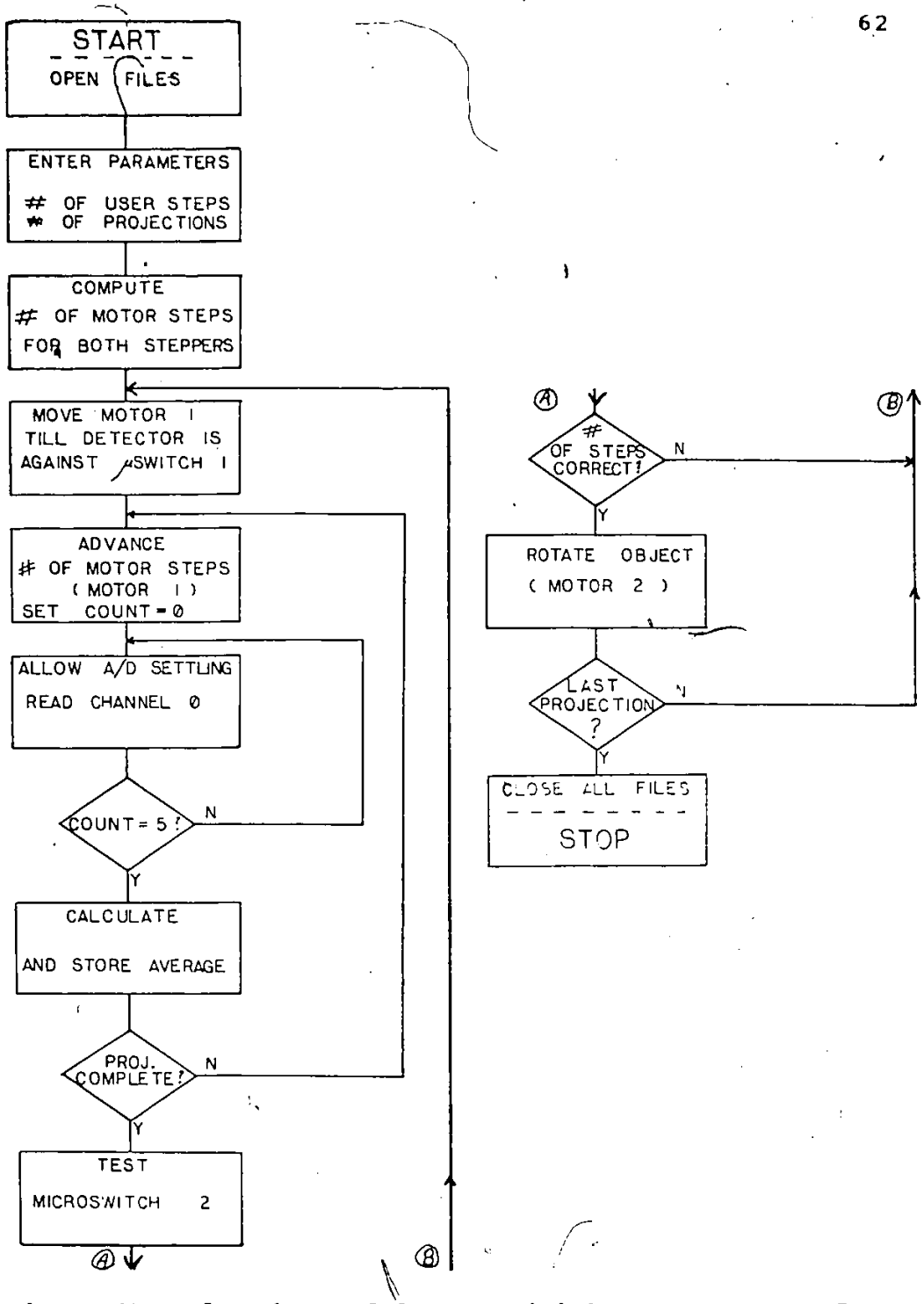

Figure 14: Flow chart of data acquisition program (ACQUIRE)

The present needs of the MCT-I system are to acquire and display one projection at a time. This is required to get an insight on the properties of wave propagation within the plates. Therefore, the data acquisition, calibration and display is performed one projection at a time. Presently, a command file (EXPMT.CMD) performs these tasks sequentially (see Fig. 15).

The first thing the command file does is to execute ACQUIRE for 1 projection. It then asks the operator if calibrated data is required. If so, the empty plate characteristics are subtracted from the projection data. The operator is then asked which display device is desired and one of the following programs is executed: GRAPH5.FTN for the HP7201 plotter or GRAPH6.FTN for the VT55 graphics display.

Figure 16 shows a flow chart of the program GRAPH6.FTN which displays a single projection of data on the VT55 graphics terminal. The operator normally chooses this display since the results are available to him immediately after the scan is complete, whereas the plotter is much slower. However, the VT55 display has 256 lines by 512 points so that the resolution is much lower than the HP plotter which has 10^4 x 10^4 points.

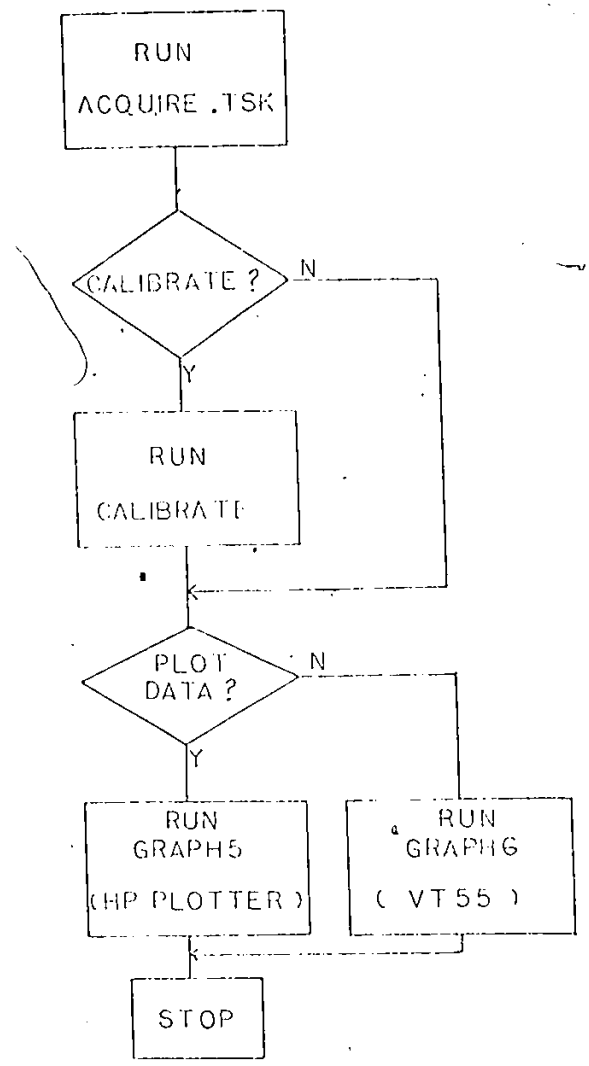

NOTE: DISPLAY ONE PROJECTION AT A TIME

Figure 15: Experiment Command File

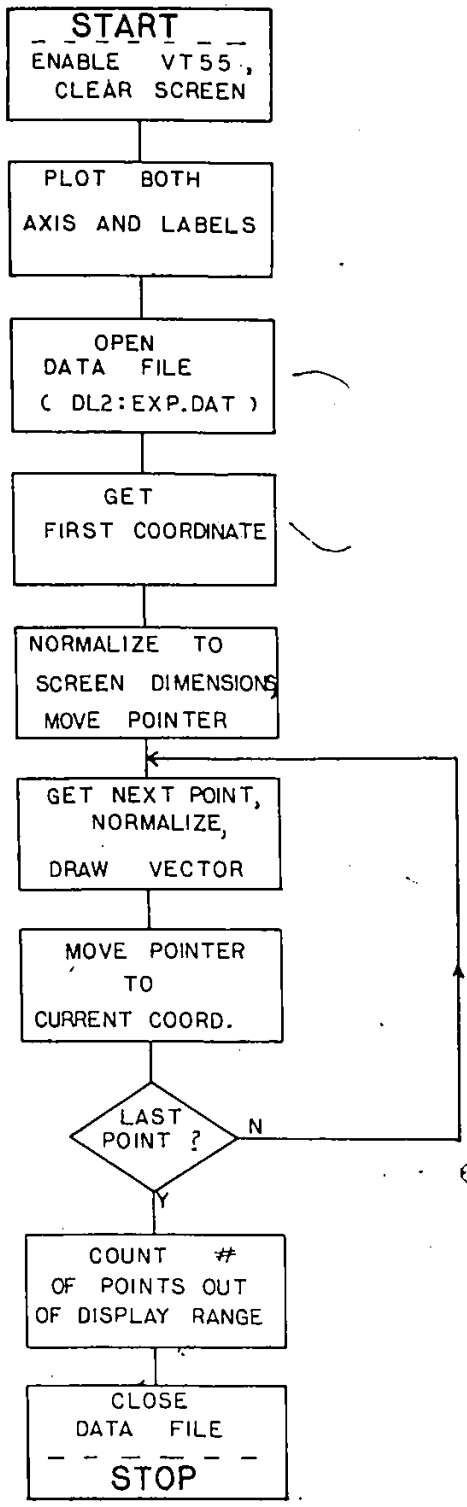

Figure 16: Flow Chart of GRAPH6.FTN (VT55 display)

The HP plotter, which accepts data in the EBCDIC format, requires a separate driver tc convert the data before transmission. The driver contains a set of subroutines which perform the fundamental requirements of a plotter; namely PLOT.FTN which plots a single point, DRAW.FTN which accepts an array of pcint ccordinates and plots them, PRT.FTN which draws alphanumeric characters and TRANS.FTN which transforms the data into EBCDIC and sends it to the plotter. The plotter is ccnnected through a 600 baud line so that it is much slower than the VT55; hence, it is only used when the operator needs a hard copy of the result. Figure 17 is a flow chart of the program GRAPH5.FTN.

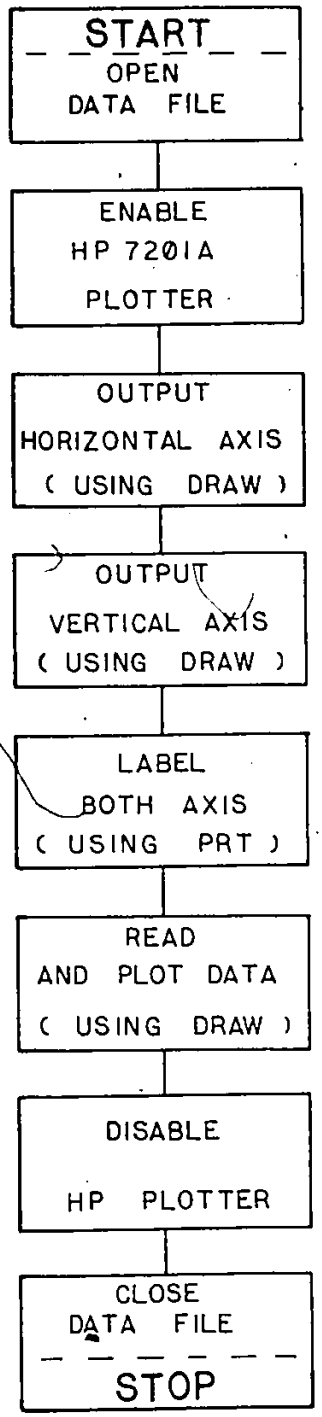

HP DRIVER ROUTINES

TRANS : TRANSMIT DATA

PLOT : PLOT POINT

DRAW : PLOT MANY POINTS

PRT : PRINT ALPHANUMERIC CHARACTERS

Figure 17: Flow Chart of GRAPH5.FTN (HP7210 plotter)

Chapter V

RESULTS

This chapter presents the initial results obtained using the MCT-I system. These include the empty chamber characteristics, scattering from metal cylinders and projection data for a few dielectric cylinders. Also included are reconstructions of simulated X-ray data; they are performed to test the reconstruction algorithms which could possibly be modified for MCT at a later date.

5.1 EMPTY PLATE CHARACTERISTICS

In order to evaluate the performance of the chamber, a parameter of interest is the Standing Wave Ratio (SWR) measured at the horn and detector for various frequencies. These SWR measurements give a measure of the propagation of energy from, respectively, the horn to the chamber or from the chamber to the detector. Figures 18 and 19 give the SWR measured at the horn and detector respectively. These measurements are made at frequencies swept from 8-12 GHz. One can see that the SWR at the horn is well below 10-dB for most frequencies between 8 and 12 GHz. This implies that 90% of the energy propagates from the horn to the chamber indicating a relatively good match.

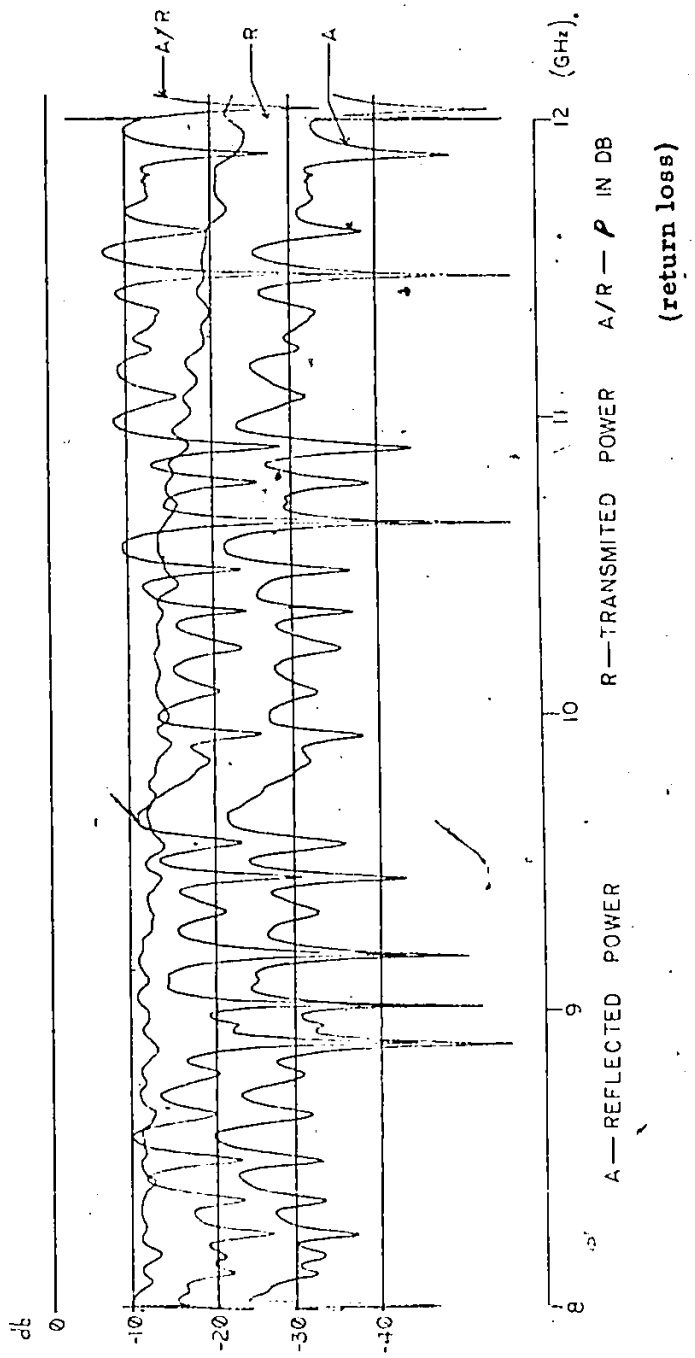

Figure 18: SWR of horn for frequencies 8-12GHz

Figure 19 is the SWR measured at the detector as the frequency is swept from 8-12 GHz. It is found to be relatively independant of position as the detector is moved from one end of the observation plane to the other. One can see that a good match only occurs at specific frequencies; namely, 8.6, 9.4, 10.2, 11 and 11.9 GHz. Operation is therefore presently limited to those frequencies so that a maximum amount of energy may propagate from the horn to the detector.

The quality of the chamber can also be evaluated quickly by examination of the projection data obtained with the plates empty. This gives an indication of the amount of internal reflections in the chamber as well as the radiation pattern of the antenna. A number of these measurements are taken at various frequencies and resolution settings of the swept amplitude analyser. Figure 20 shows the empty chamber characteristics at 10.2-GHz with a resolution of 1-dB/cm on the swept amplitude analyser. The horizontal axis is labelled in cm from the center of the observation plane. The half-power beam width can be seen to occur at approximately ±17cm. Since the observation plane is 1.2 m from the phase center of the source, this translates into a 16° beamwidth, which agrees with the value obtained in the design of the horn.

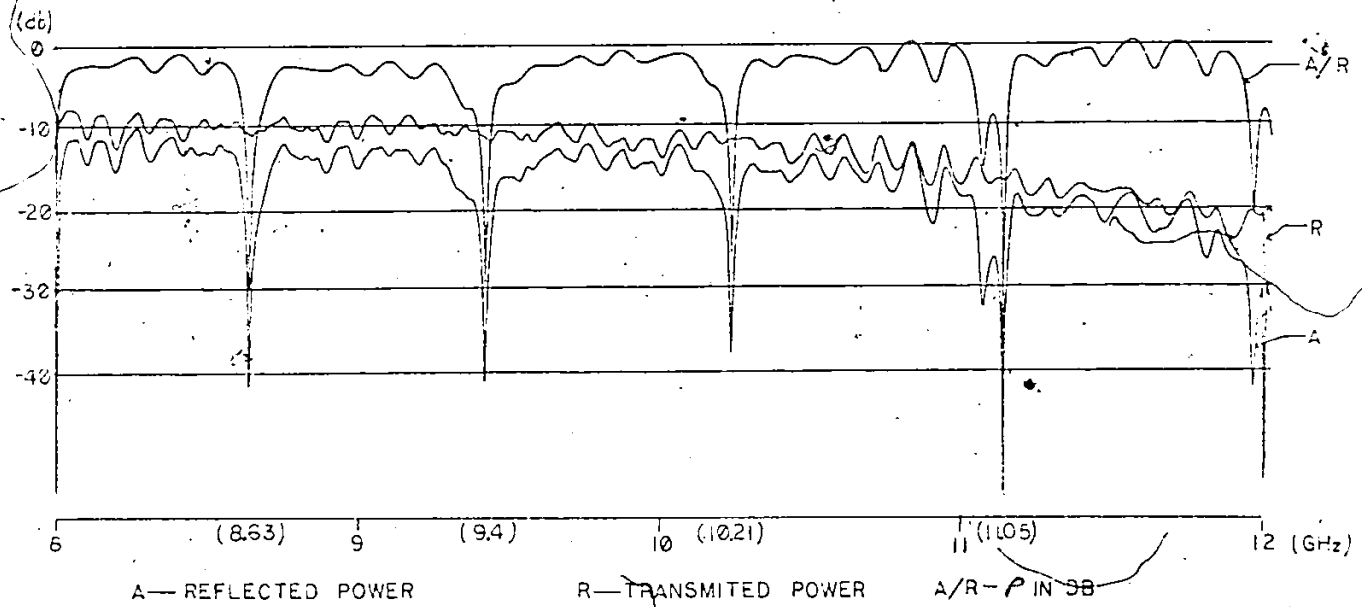

Figure 19: SWR of detector for frequencies 8-12 GHz

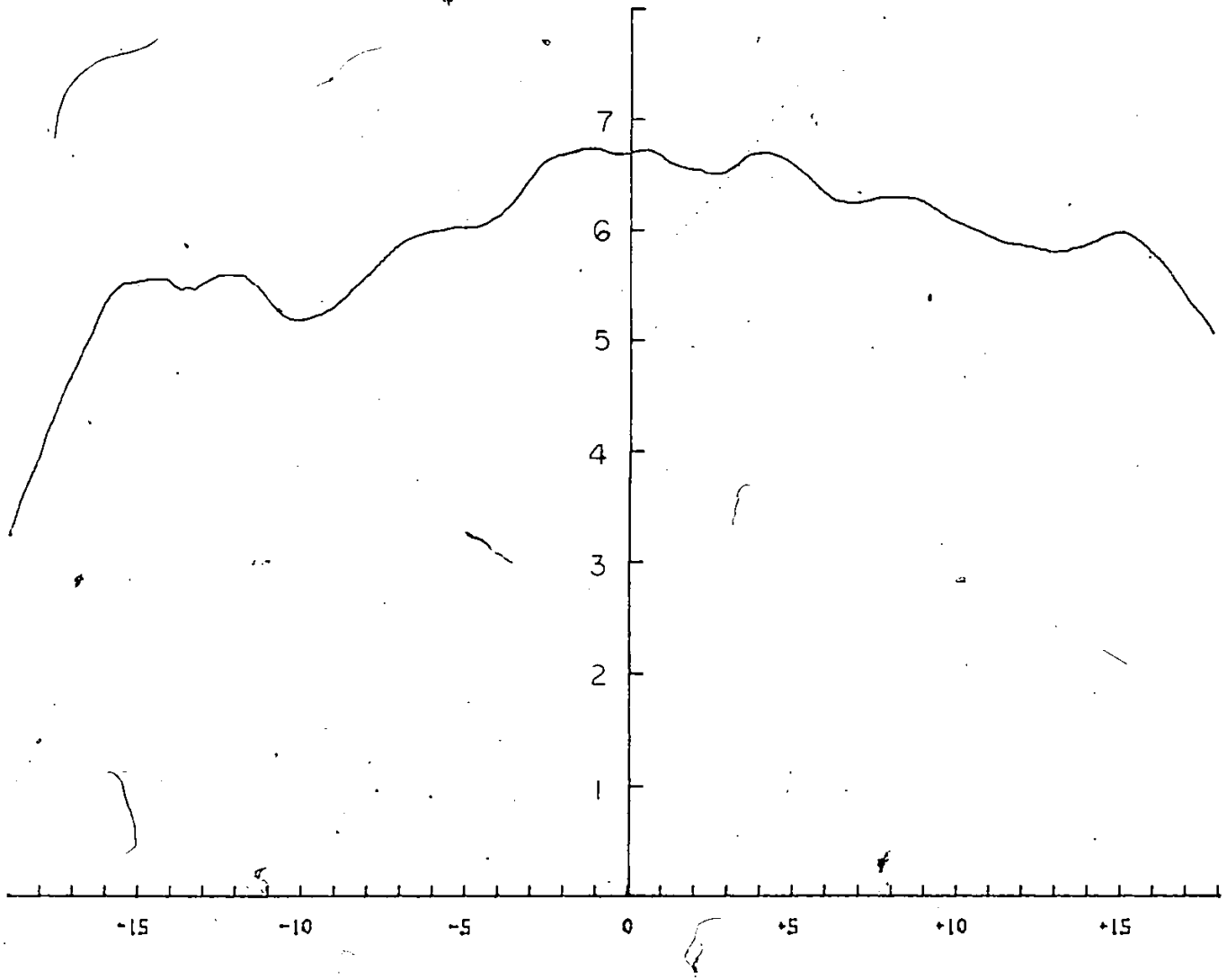

Figure 20: Empty-Chamber measurement (1dB/cm), f=10.2 GHz

This graph shows the field distribution at the end of the plates. It shows that with no object present in the plates, the field is relatively smooth (±0.75 dB's).

Figure 21 is essentially the same as Fig. 20 except that the resolution of the swept amplitude analyser is 5-dB/cm. This is the scale most frequently used experimentally since scattering from typical objects create a perturbance of the order of 15-dB. Figure 22 is the same measurement except the frequency is decreased to 8-GHz from 10.2-GHz. The variation in frequency alters the position and amplitude of the "oscillations" in both curves. These fluctuations are of the order of 0.5-1 dB (see Fig. 20) and are due to reflections from the walls of the chamber as well as to the non-uniform radiation pattern of the sectoral horn. Their magnitude being of the order of 1-dB, a relatively large SNR is obtained with scatterers that perturb the electric field in the order of 15-dB.

The pattern obtained with the empty chamber is relatively uniform as seen in Fig. 21. This plot is now used as a calibration curve for measurements made at 10.2-GHz. By subtracting this curve from the scattered electromagnetic field from an obstacle, it will approximate the measurement of a scattered electric field due to the obstacle only.

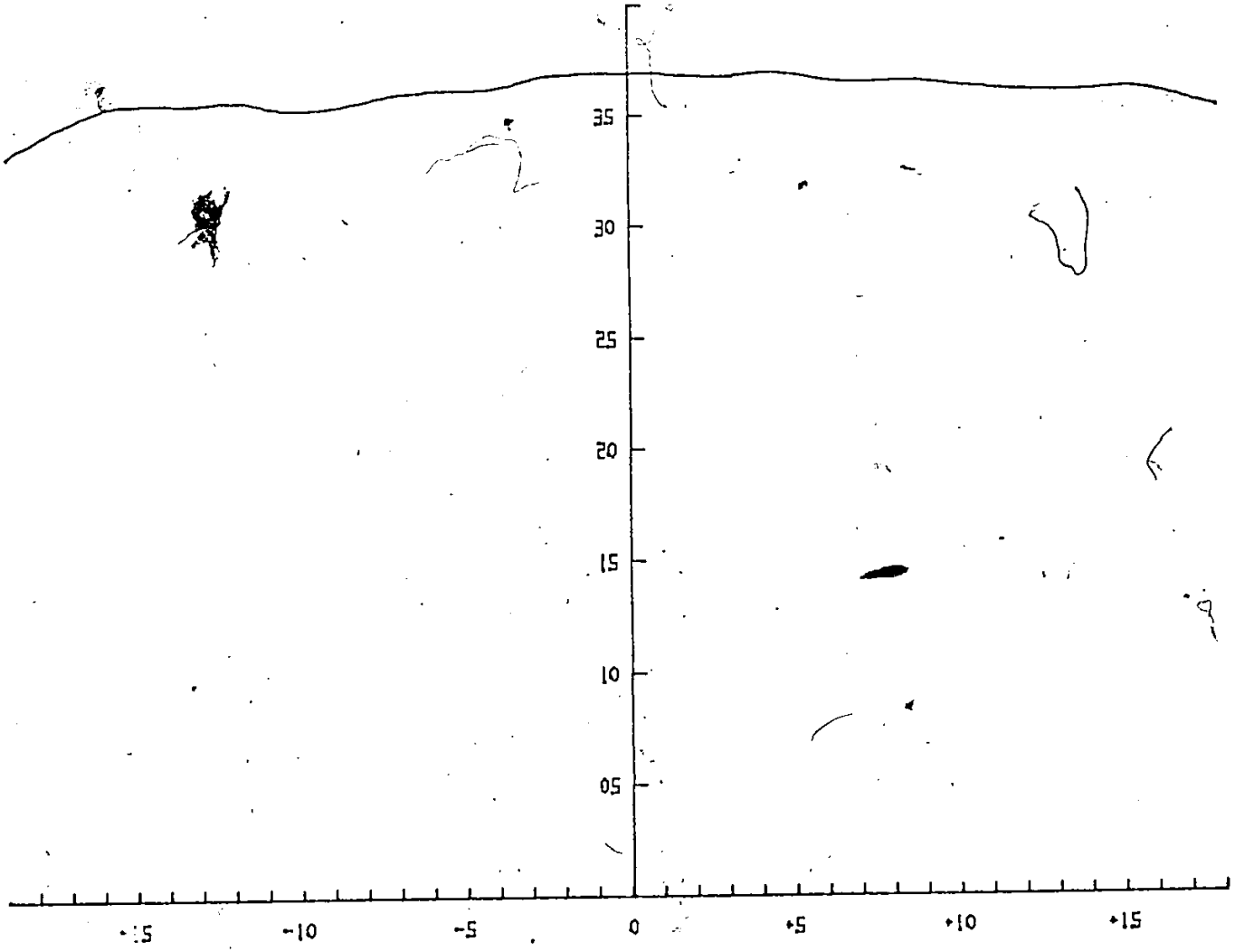

Figure 21: Empty-Chamber measurement (5dB/cm), f=10.2 GHz
This curve is essentially the same result as in Figure-20. The difference being that the resolution of the swept amplitude analyser is set at 5 dB/div. This is now the calibration

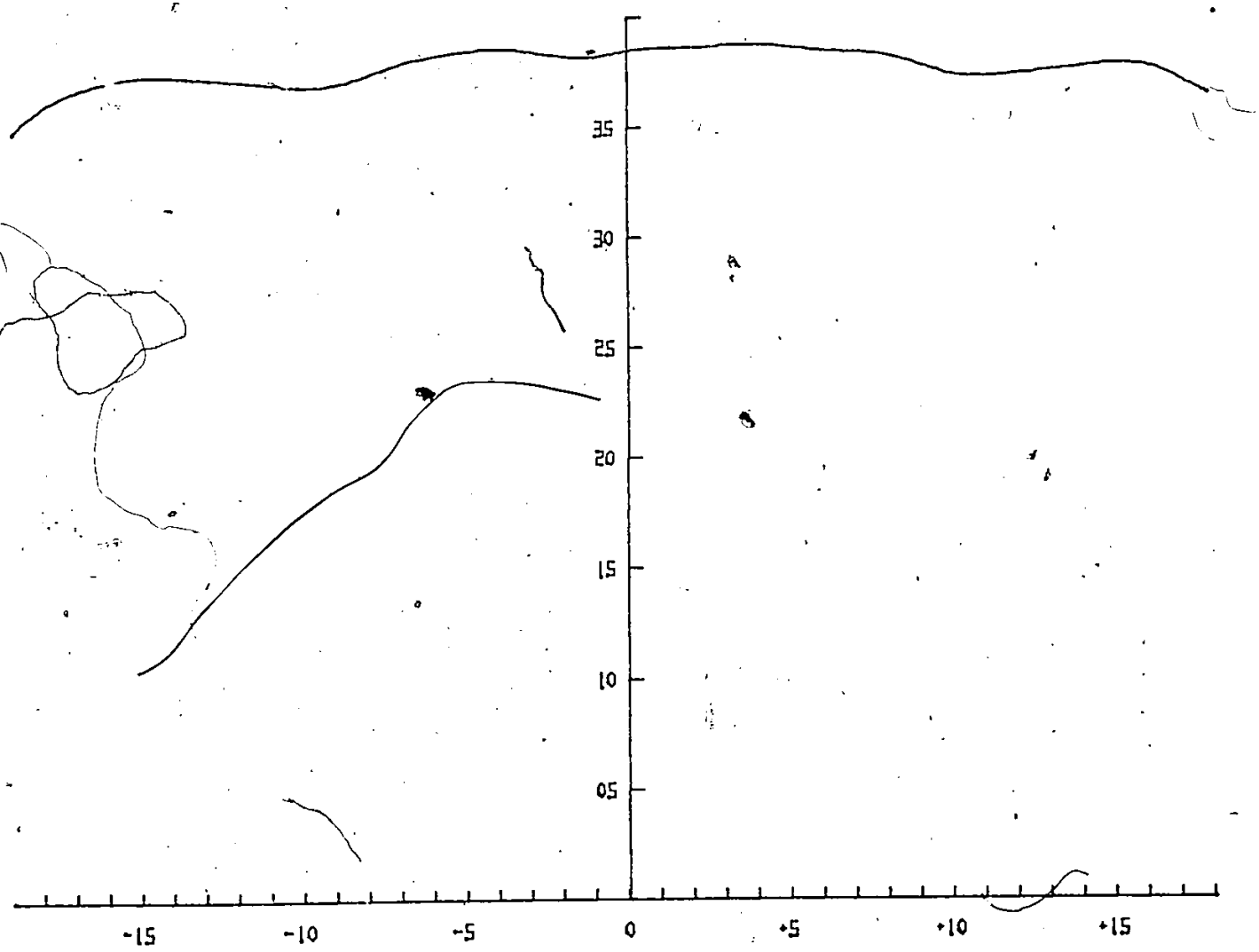

Figure 22: Empty-Chamber measurement (5dB/cm), f=8 GHz
This is the same measurement as in Figure-21 except that it is performed at a different frequency. The displacement of the small ripples indicate that they are due to the radiation pattern of the horn and to internal reflections.

5.2 SCATTERING FROM METAL CYLINDERS

The purpose of including measurements of scattered fields from metal cylinders is to verify the performance of the chamber. This is because the scattered field from metal cylinders is well known; its theoretical derivation is included in appendix-A. All measurements in this section are performed at 10-GHz so that the free space wavelength (3 cm) is an exact divisor of the diameters of three metal disks that were made (3,6 and 9 cm).

The first measurements were performed on the metal disk 3 cm in diameter (1 wavelength). Figure 23 shows the scattered field from the metal disk when it is placed 111.0 cm from the phase center of the source. The "smooth" curve, which is the corresponding theoretical result, agrees with the experimental result to within ±0.75dB. As can be seen, the typical perturbation of the field is quite large in relation to the non-uniformities of the calibration curve of Fig. 21. Figure 24 shows the scattered field from the same disk when it is placed 87.0 cm from the source. In this case, only the first "cycle" of the diffraction pattern is seen and once again, agreement with theory is within 1-2 dB.

Figures 25 and 26 show scattering from metal disks respectively 6 cm and 9 cm in diameter (2 and 3

wavelengths). In both cases, the disk is placed at a distance of 111.0 cm from the phase center of the source. The theoretical curves (smooth curves) once again agree relatively well with the experimental results.

The experimental results of the 4 scatterers used conform relatively well to the theoretical results. This holds true for obstacles creating a 5-dB perturbance as well as one creating a 35-dB perturbance. The chamber is therefore of sufficient quality so that scattered fields of this order of magnitude can be accepted as correct. For attenuations larger than 35-dB's, the intensity of the reflections from the walls may dominate over the actual scattered field so that the results would be falsified. However, the 40-dB dynamic range of the MCT-I system eliminates the possibility of this problem.

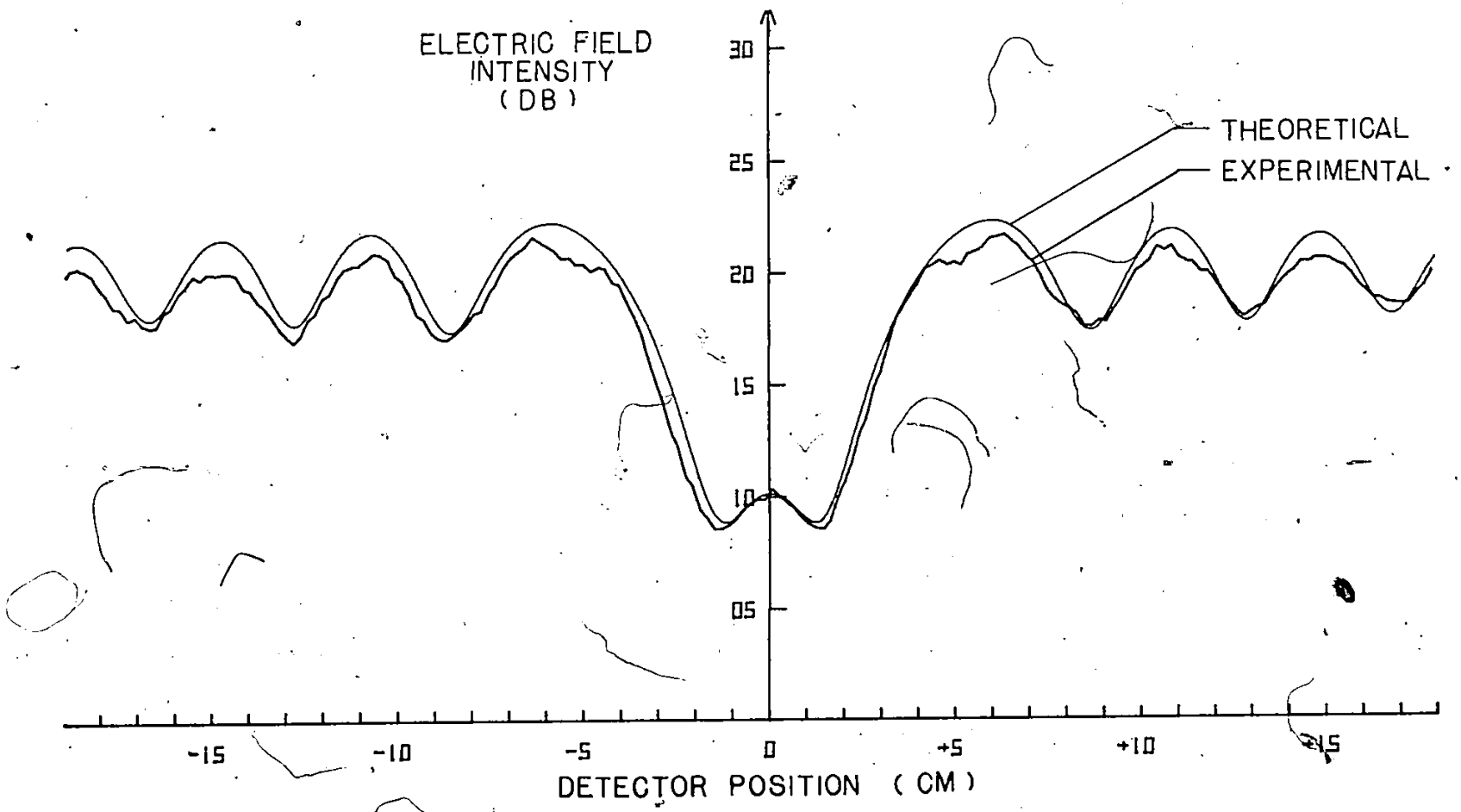

Figure 23: Scattering from 3 cm metal disk, D=111.0 cm
The metal disk is placed 111.0 cm from the phase center of the source. It is in good electrical contact with both metal plates.

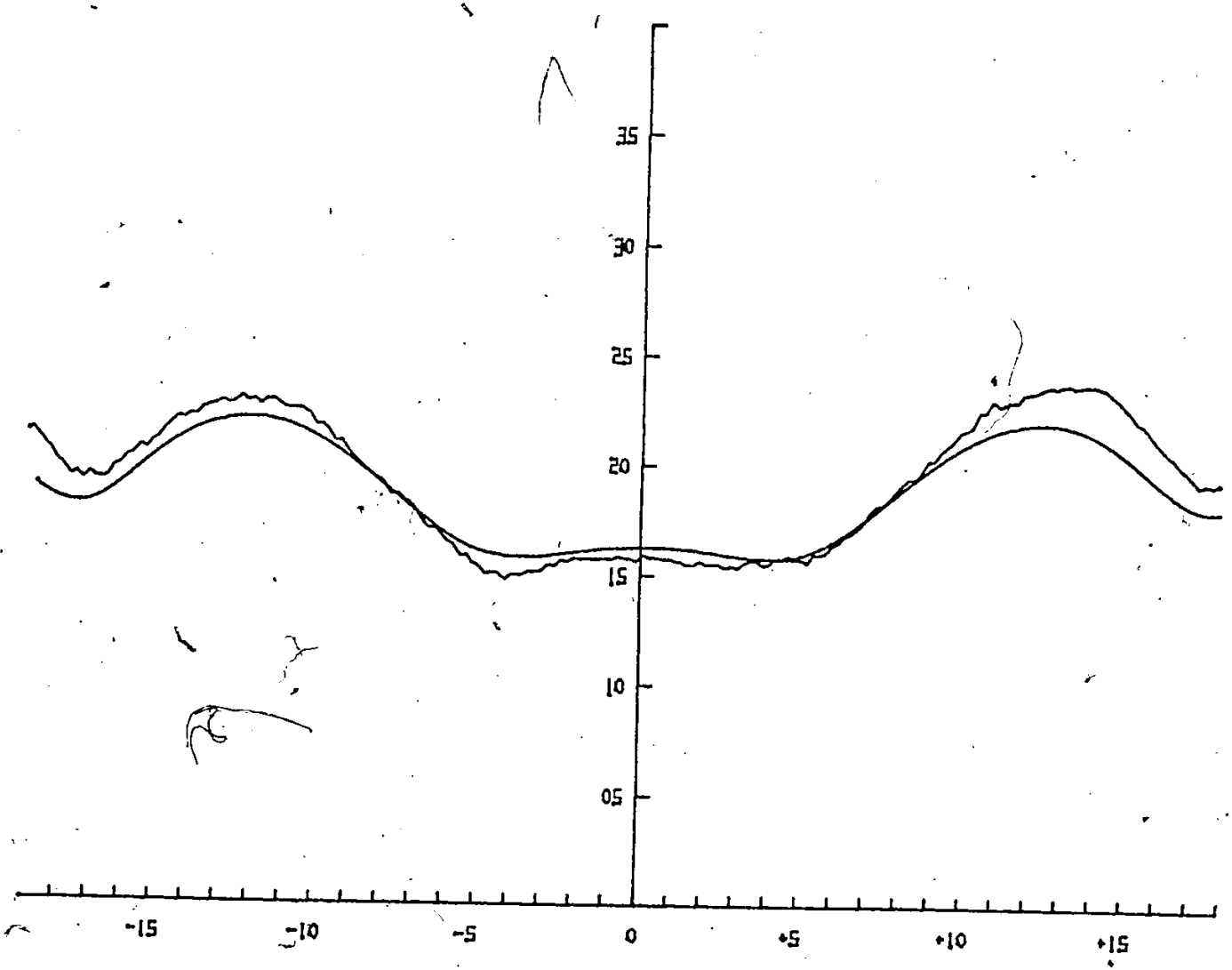

Figure 24: Scattering from 3 cm metal disk, D=87.0 cm

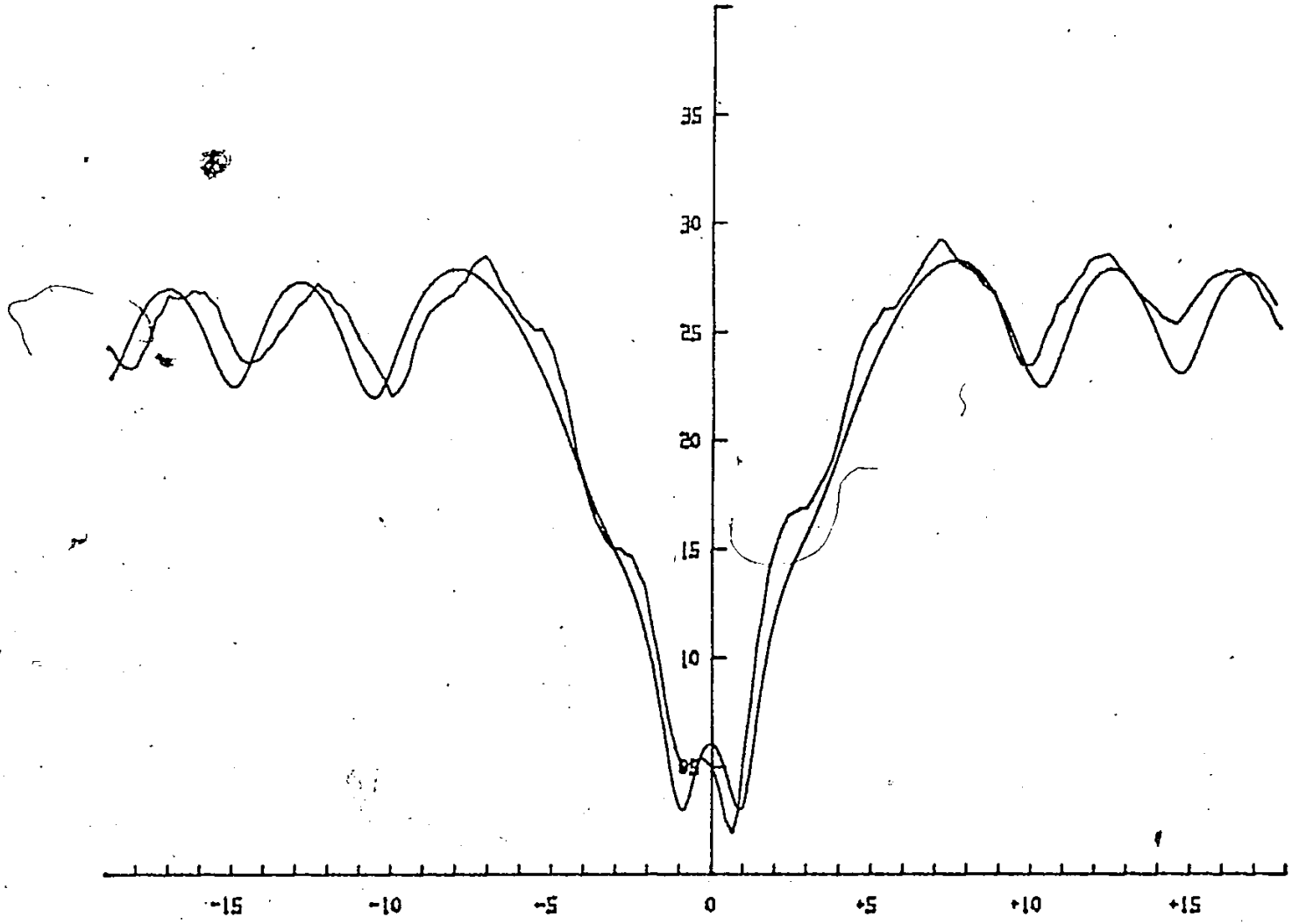

Figure 25: Scattering from 6 cm metal disk, D=111.0 cm

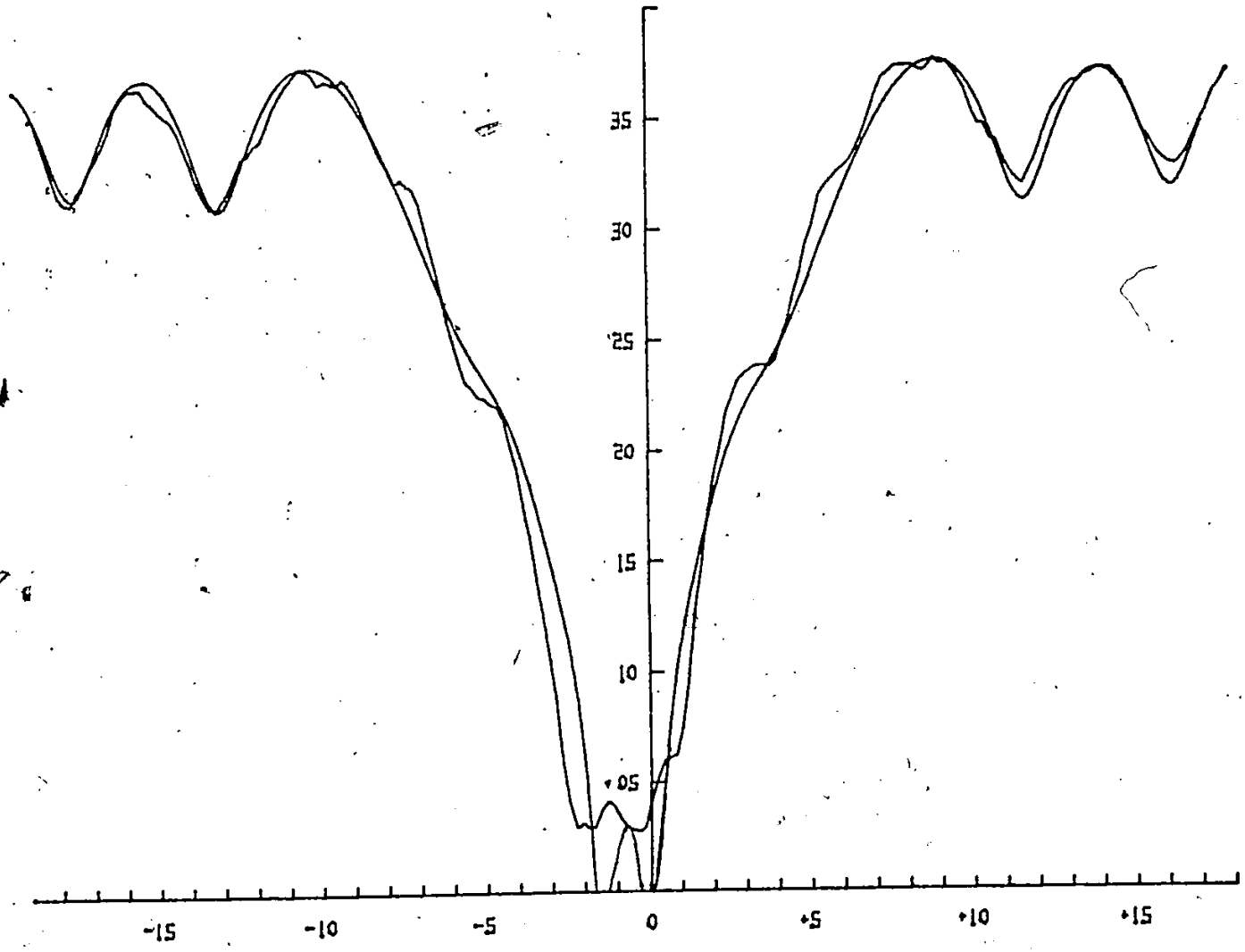

Figure 26: Scattering from 9 cm metal disk,D=111.0 cm

5.3 SCATTERING FROM DIELECTRIC MATERIALS

This section includes initial measurements on dielectric materials. The objects studied are made of high-density polyethylene or of a fat phantom. The attenuation constant of polyethylene can be found in chapter 3, whereas that of the fat phantom is 2 dB/cm. The object configurations used are either a 3 cm disk or a large 15 cm disk with a 3 cm hole offset from the center. Various objects were studied by using different combinations of large disk with a smaller disk inserted in it. The scattering characteristics included in this section have all been done at 10.2-GHz and have not been verified mathematically as in the case of metal cylinders.

An additional test of the performance of the chamber is done by verifying the symmetry of the measured electromagnetic field for symmetrical objects. The model utilized is that of a 15 cm diameter fat phantom disk with a 3 cm diameter metal disk inserted in it. Figures 27 and 28 show the actual object positions in relation to the incident wave along with their respective scattering characteristics. As can be seen, both curves are mirror images of one another (to within a few dB's) as expected. In this instance, the small discrepancies may be due to positional errors within the chamber as well as to a 2 dB offset difference on the swept amplitude analyser.

Other measurements of scattered fields from dielectric cylinders are shown in Fig. 29, 30, 31 and 32. Figure 29 is the scattering from a 15 cm diameter polyethylene disk. The two "dips" are due to the diffraction at the air/disk interface; they are found to vary in position and amplitude as the disk is moved in the chamber along the source-detector line. Lytle [28] made use of these dips to determine the shape and location of tunnels and he obtained satisfactory results. Figure 30 shows the scattering from the 15 cm fat phantom disk. The first observation that can be made is the expected attenuation behind the disk compared to the non-lossy polyethylene. The actual pattern obtained is once again the characteristic "signature" of the interfering scattered fields.

Figures 31 and 32 show the measured fields scattered from the 3 cm polyethylene disk placed inside the fat phantom disk for two different positions. The significance of the difference in the curves is that two separate signatures are obtained with objects of differing internal structure. Although the mathematics of this problem are not solved, this is an encouraging result.

Many other measurements were also performed, a few of which are included in appendix-B.

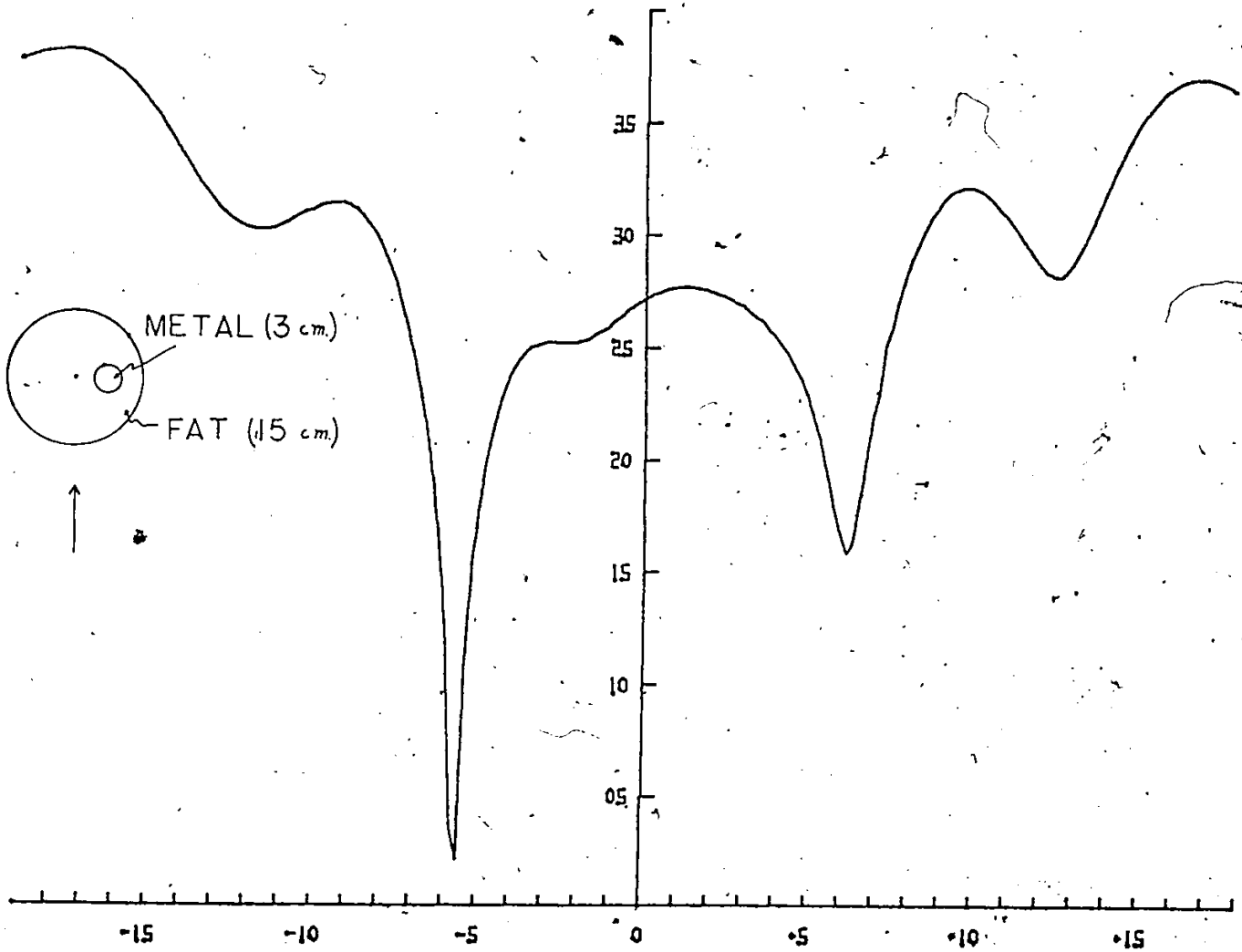

Figure 27: Scattering from metal in fat, D=87cm, θ=90°

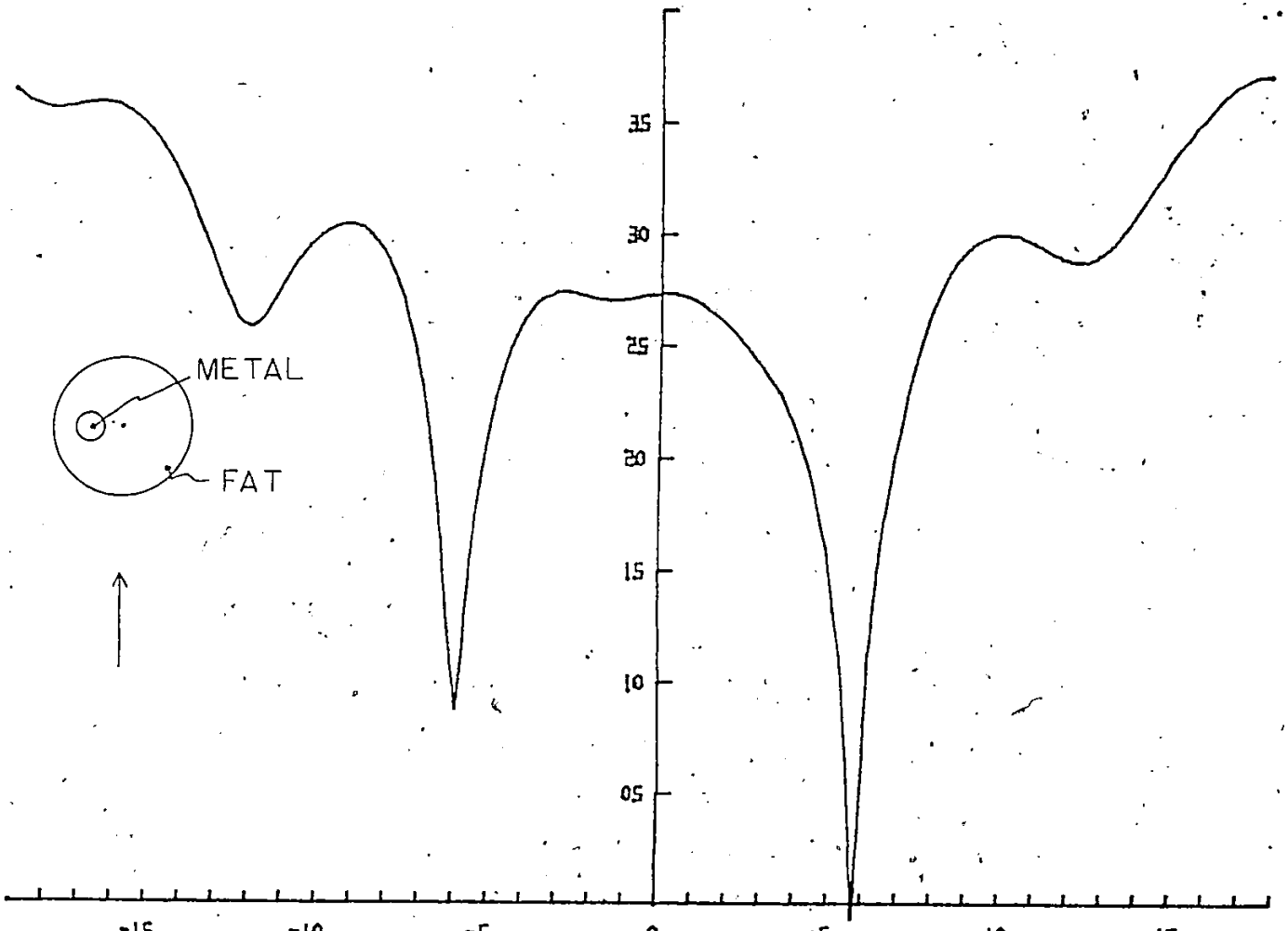

Figure 28: Scattering from metal in fat, D=87cm, θ=270°

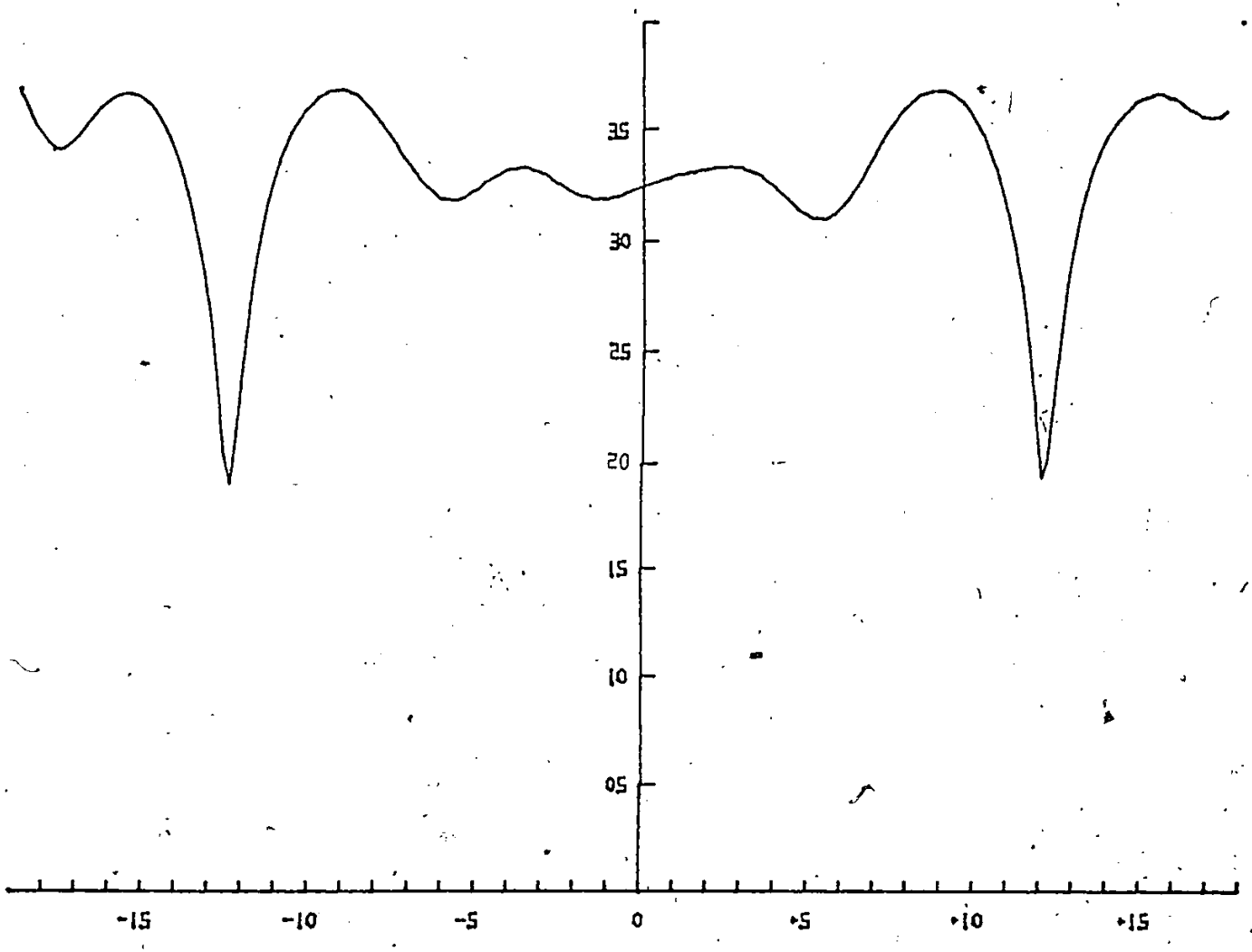

Figure 29: Scattering from 15 cm polyethylene disk, D=110cm

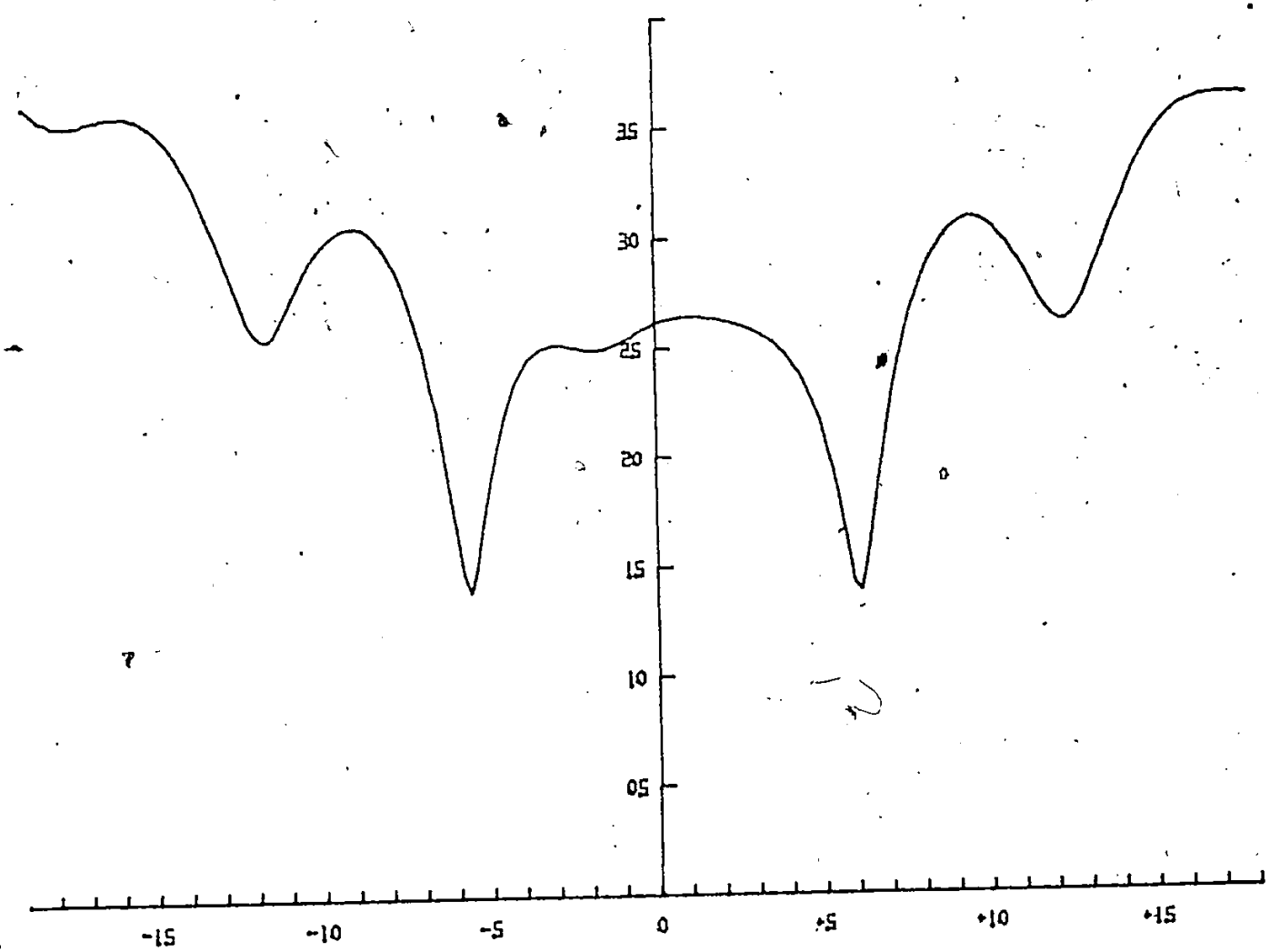

Figure 30: Scattering from 15 cm fat phantom disk, D=110cm.

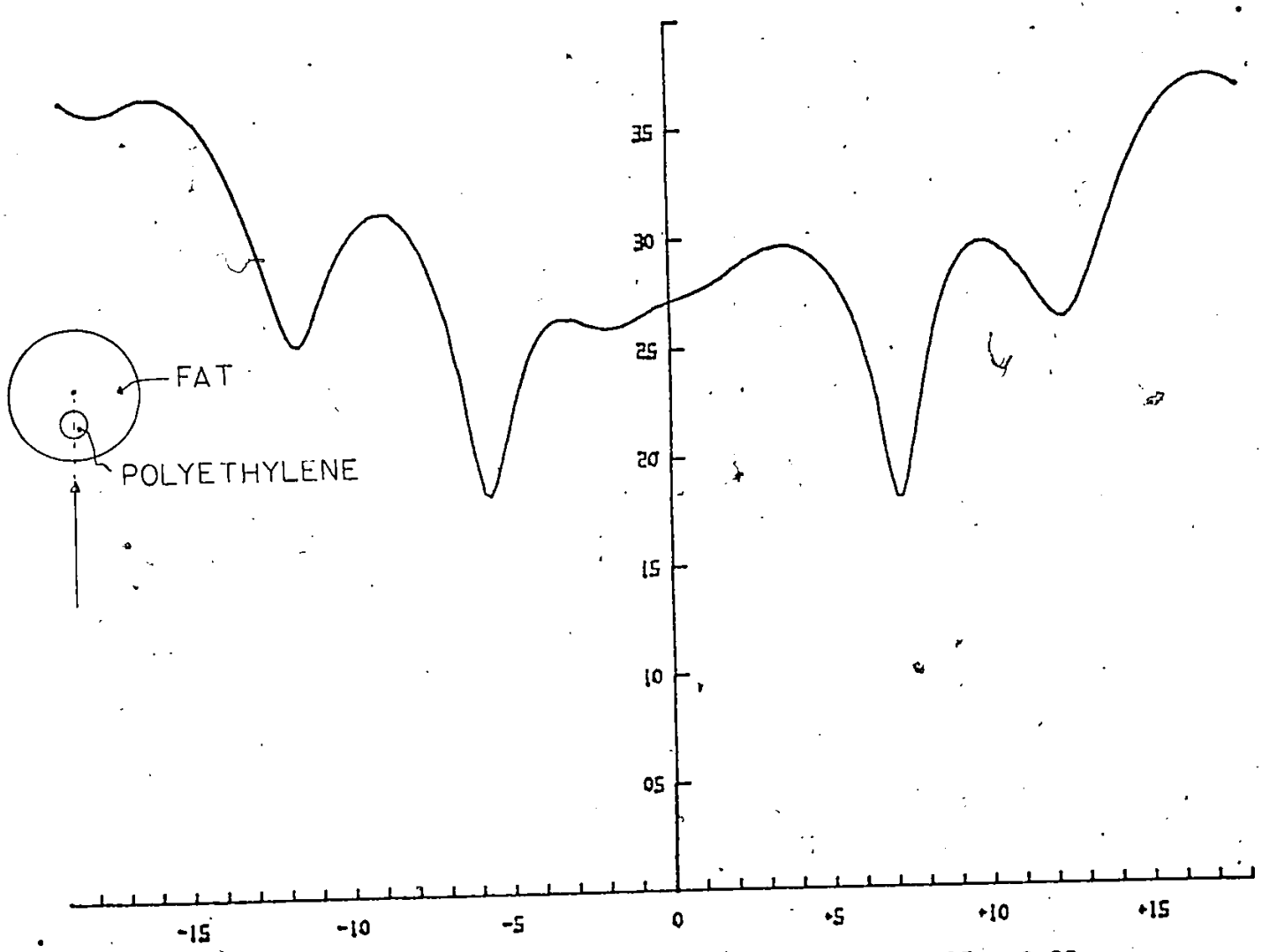

Figure 31: Scattering from polyethylene in fat, D=87cm, θ=0°

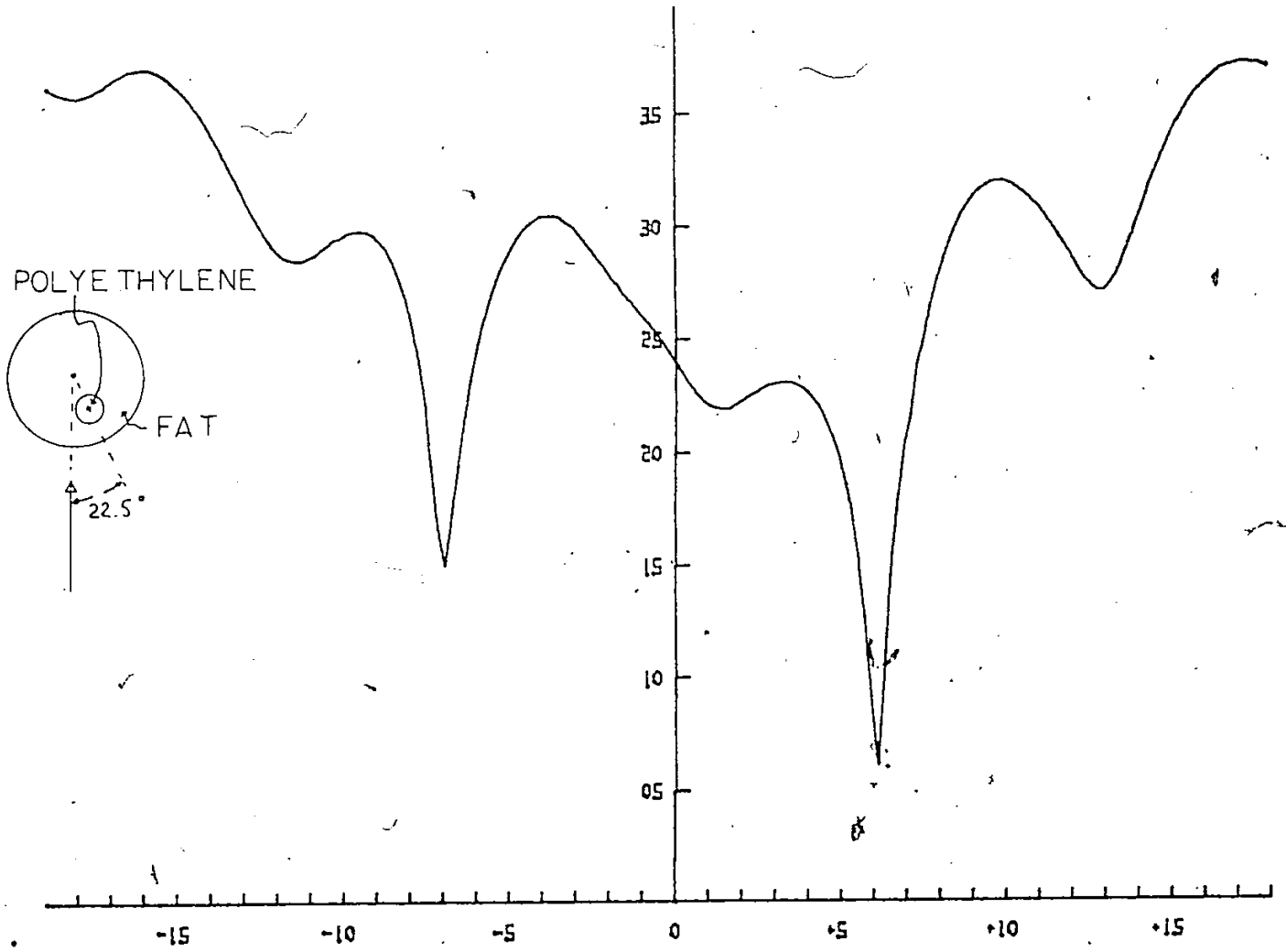

Figure 32: Scattering from polyethylene in fat, D=87cm, θ=22.5°

5.4 RECONSTRUCTIONS OF SIMULATED X-RAY DATA

The results shown in this section are reconstructions of X-ray data simulated on the PDP11 minicomputer. The algorithms implemented are that of ART and convolution. They are tested with varying degrees of additive gaussian noise (AGN). While they cannot be used directly on data collected with the MCT-I system, perhaps they can be modified to operate on projections obtained from a refraction dominant object. This type of propagation could possibly occur if the worst case mismatch between any two points in the chamber is small such that the refraction effects dominate over diffraction effects.

The ART algorithm implemented uses the length of rays through individual pixels as the weight applied in the correction factor. Figure 33 is a flow chart of the ART algorithm. Figure 34 shows the reconstruction of a model with no noise and 2 levels of AGN. The model consists of muscle with a circular bone offset from the center to eliminate circular symmetry. It can be seen that even at 10% AGN, the bone can still be distinguished.

Another algorithm implemented is the convolution algorithm. Figure 35 is a flow chart of this reconstruction algorithm; it is a direct implementation of the technique described in the section on convolution. Figure 36

demonstrates the effect of varying the number of projections of noiseless data to reconstruct the same model as in ART.

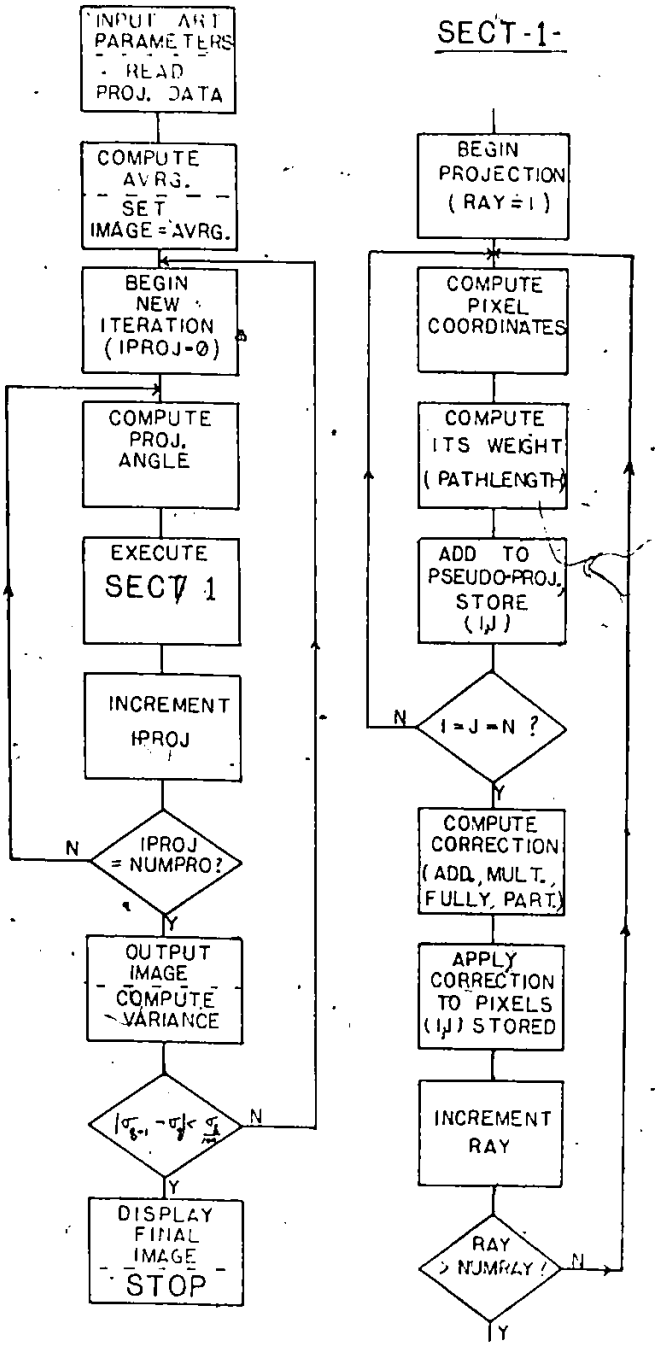

Figure 33: Flow chart of ART algorithm

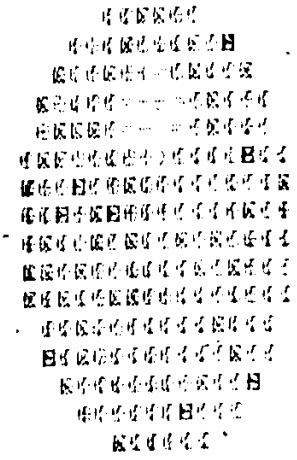

a) Reconstruction using unconstrained multiplicative ART.

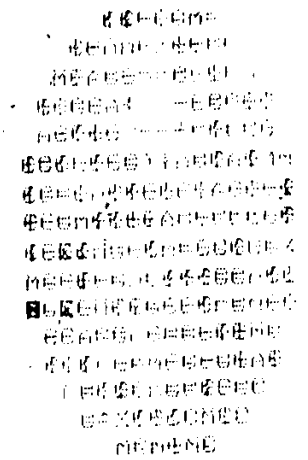

b) Same as a) but with 3% gaussian noise added to data.

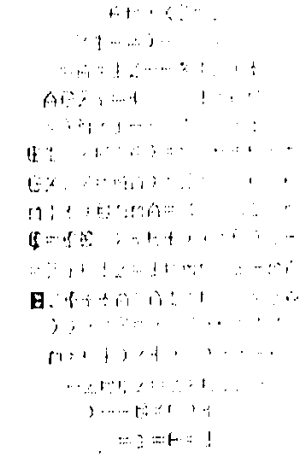

c) Same as a) but with 10% gaussian noise added to data.

Figure 34: Reconstruction of muscle/bone with 3 levels of AGN

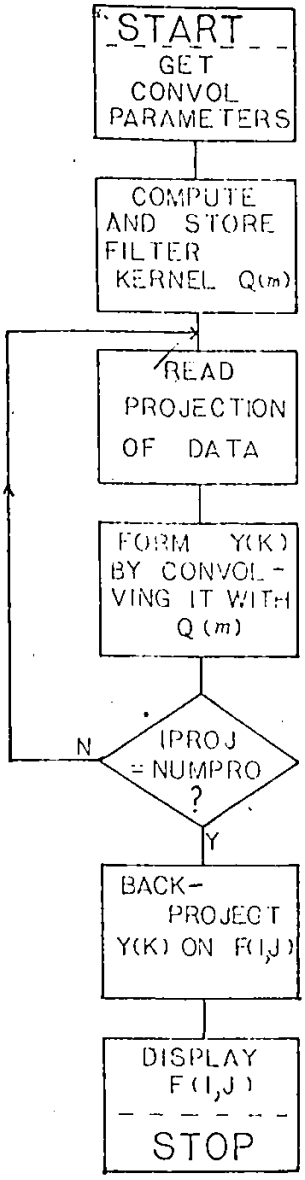

Figure 35: Flow Chart of convolution algorithm

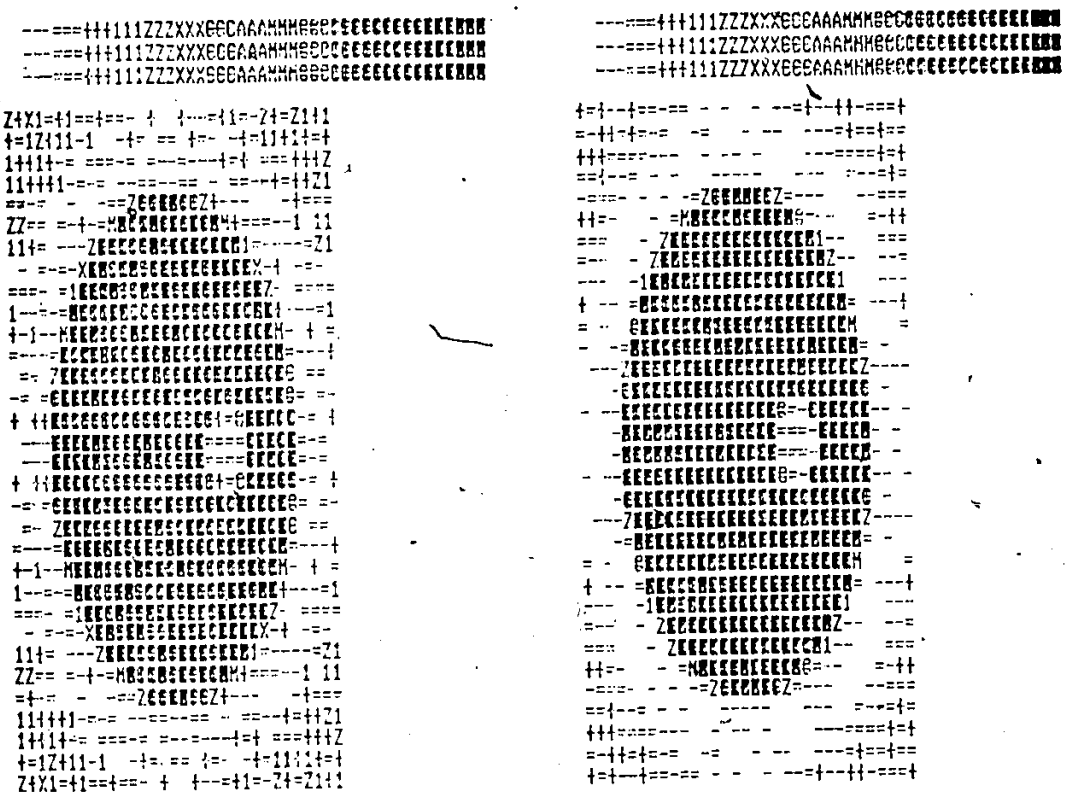

a) 32 projections

b) 64 projections

Figure 36: Effect of finite number of projections

Chapter VI

CONCLUSIONS AND FUTURE DIRECTIONS

6.1 FUTURE DIRECTIONS

Since this is a new area of investigation, it offers limitless possibilities for future research. One obvious recommendation is to incorporate phase measurements in the system. This would allow the user a possibility of recording a complete phase-amplitude hologram of the scattered field. Once these measurements are incorporated in the system, the next step involves the analysis of diffraction and more precisely, the solution to the inverse scattering problem. In order to take diffraction into consideration, there are basically two approaches that can be used. One is the minimization of diffraction while the other involves its utilization.

6.1.1 Minimization of Diffraction

The obvious way to minimize diffraction is to use the instrument only with objects containing slowly varying dielectric properties. In this way, the mismatch between any two points lying in the chamber is small. One drawback of this method however, is that most objects that one wishes

to image do indeed have significant changes in dielectric properties which the operator cannot alter to suit the instrument.

Diffraction can also be minimized by matching the source and detector to the object under study. In the experiments performed so far with the MCT-I system, the greatest change in attenuation constant occurs at the air-object interface. Although the diffracted field at this interface gives information about the interface, it is seldom useful since the external geometry of the object is already known. By eliminating the contribution of scattered fields from this interface, perhaps small perturbation theory would hold within some objects and the problem can thus be simplified.

Another method that can be used to decrease diffraction is to increase the frequency of the source. This reduces the ratio of wavelength to object dimensions. This approaches an interesting portion of the spectrum; that of microwave-infrared radiation. However, sophisticated instrumentation would be required to operate at these higher frequencies.

6.1.2 Utilization of Diffraction

This alternative is somewhat more complicated. It involves the rigorous mathematical solution of the wave

propagation problem. The formulation of the solution of the inverse scattering problem would have to include all aspects of wave propagation, including higher order modes of propagation if they occur.

Information about a larger portion of the scattered field may also be necessary. Presently, the MCT-I system can only measure a 16° section of the scattered field. It may prove necessary to construct a circular chamber with detector motion covering a wider angle.

6.2 CONCLUSIONS

The performance of the MCT-I system is quite satisfactory for the purpose of studying two-dimensional electromagnetic scattering. The use of a parallel-plate chamber provides an excellent method of simplifying the geometry of the problem. In addition, the ability to perform measurements of scattered fields quickly and under computer control makes the MCT-I system a powerful research tool.

An examination of the field distributions included in chapter 5 indicate that simple geometrical optic theory cannot be used to interpret the results. Therefore, the original hypothesis of ray tracing in the object cannot be applied here. It seems apparent that resolution of the order of one wavelength with objects containing sharp

discontinuities can be obtained only by consideration of the complex diffraction model. Perhaps only objects composed of substances having relatively uniform dielectric properties can be reconstructed with the use of ray tracing. Therefore, a good mathematical model of diffraction appears to be the solution to the inverse scattering problem, and the MCT-I system is capable of providing a quick, efficient means of measuring these scattered fields accurately.

The topic discussed in this thesis, which is the design and testing of an MCT device, is a very interesting area of engineering physics. The exact solution of the inverse scattering still remains unsolved. However, the construction of the first version of an MCT system has provided an insight on the problem and the experience gained may prove invaluable in the design of a later version of the instrument. It would appear that this second version must have a wider angle of view, perhaps as much as 180°, along with matching of the surrounding medium to the object by immersing the object in liquid. These additional constraints may provide a larger portion of the scattered field which would not contain any contributions from the external interface of the object.

Appendix A

SCATTERING FROM METAL CYLINDERS

The extent to which the instrument approaches ideal performance is best determined with a problem in electromagnetic scattering that can be solved exactly. Probably the simplest boundary condition that one can have is that of a cylindrical metal obstacle[3]. This appendix gives the derivation of the theoretical expression for scattering from metal cylinders of different radii.

The equation describing a parallel wave is the same form for sound as for electromagnetic waves and is given by:

$$e^{2\pi iv/c\cdot(x-ct)} = e^{2\pi iv/c\cdot(r\cos\phi - ct)} \qquad (A.1)$$

This parallel wave can be expressed as a sum of circular waves:

$$e^{2\pi iv/c\cdot(x-ct)} = \sum_{m=0}^{\infty} A_m \cdot \cos(m\phi)\cdot J_m(2\pi vr/c)\cdot e^{-2\pi ivt} \qquad (A.2)$$

---

[3]P.M. Morse, "Vibration and Sound", McGraw-Hill, N.Y., 1942, pp.191-200, 346-370.

After computing the coefficients A_m, one gets the following expression for the wave:

$$e^{2\pi iv/c(x-ct)} = \{ J_0\left(\frac{2\pi vr}{c}\right) + \sum_{m=1}^{\infty} 2i^m \cos(m\phi) \cdot J_m\left(\frac{2\pi vr}{c}\right) \} e^{-2\pi ivt} \quad \text{(A.3)}$$

The incident sound pressure wave can therefore be expressed in the following manner:

$$p = P \cdot e^{ik(x-ct)} = P \cdot e^{ik(r\cos\phi - ct)} \quad \text{(A.4)}$$

Using $k=2\pi v/c$ and equation (A.3), this becomes:

$$p = P\{ J_0(kr) + \sum_{m=1}^{\infty} 2i^m \cdot \cos(m\phi) \cdot J_m(kr) \} e^{-2\pi ivt} \quad \text{(A.5)}$$

The velocity of the wave can be found using Newton's law of motion:

$$v_p = \frac{1}{i\omega\rho} \cdot \frac{\partial P}{\partial r} \quad \text{(A.6)}$$

Using equation (A.5), this becomes:

$$v_p = \frac{P}{\rho c} \cdot e^{-2\pi ivt} \cdot \{ iJ_1(kr) + \sum_{m=1}^{\infty} i^{m+1} \cdot (-J_{m-1}(kr) + J_{m+1}(kr)) \cos(m\phi) \} \quad \text{(A.7)}$$

In addition to this incident plane wave, there is a scattered wave from the metal cylinder of radius a. If we

express this wave in the same manner as equation (A.2), one gets:

$$p_s = \sum_{m=0}^{\infty} A_m \cdot \cos(m\phi) \cdot \{J_m(kr) + i\, N_m(kr)\} \cdot e^{-2\pi i v t} \qquad (A.8)$$

Using equation (A.6),

$$v_s = \frac{1}{\rho c} \cdot \{A_0 \cdot i(J_1(kr) + iN_1(kr)) + \qquad (A.9)$$

$$i/2 \cdot \sum_{m=1}^{\infty} A_m \cos(m\phi)\{J_{m+1}(kr) - J_{m-1}(kr) + iN_{m+1}(kr) - iN_{m-1}(kr)\}\}e^{-2\pi i v t}$$

For the particular case of a metal cylinder of radius a, simply subject the boundary condition that the velocity at the surface (r=a) equals 0.

$$v_s + v_p = 0 \qquad \text{at } r=a \qquad (A.10)$$

Solving for A_m,

$$A_m = -\varepsilon_m \cdot P \cdot i^{m+1} \cdot e^{-(i\gamma_m)} \cdot \sin(\gamma_m) \qquad (A.11)$$

where: $\varepsilon_0 = 1$, $\varepsilon_m = 2$, $\tan(\gamma_0) = \dfrac{-J_1(ka)}{N_1(ka)}$

$$\tan(\gamma_m) = \frac{J_{m-1}(ka) - J_{m+1}(ka)}{N_{m+1}(ka) - N_{m-1}(ka)}$$

Therefore, equation (A.8) becomes:

$$p_s = - \sum_{m=0}^{\infty} \varepsilon_m \cdot P \cdot i^{m+1} \cdot e^{-(i\gamma_m)} \cdot \sin(\gamma_m) \cdot \cos(m\phi) \cdot H_m^1(kr) \cdot e^{-2\pi ivt} \quad \text{(A.12)}$$

where:

$$H_\nu^1(x) = J_\nu(x) + i \cdot N_\nu(x)$$

In electromagnetics, this transforms to:

$$E_z(r,\theta) = e^{ikr\cos\theta} - \sum_{m=0}^{\infty} \varepsilon_m \cdot i^{m+1} \cdot \sin(\delta_m(ka)) \cdot e^{-(i\delta_m(ka))} \cdot H_m^1(kr) \cdot \cos(m\theta) \quad \text{(A.13)}$$

In equation (A.13) above, the total field is expressed as the sum of the incident and scattered fields.

Appendix B

ADDITIONAL RESULTS

This section includes additional results that give good examples of scattering. Information on how the measurement is made and with which object is indicated on the diagram itself using the same format as in the chapter on results.

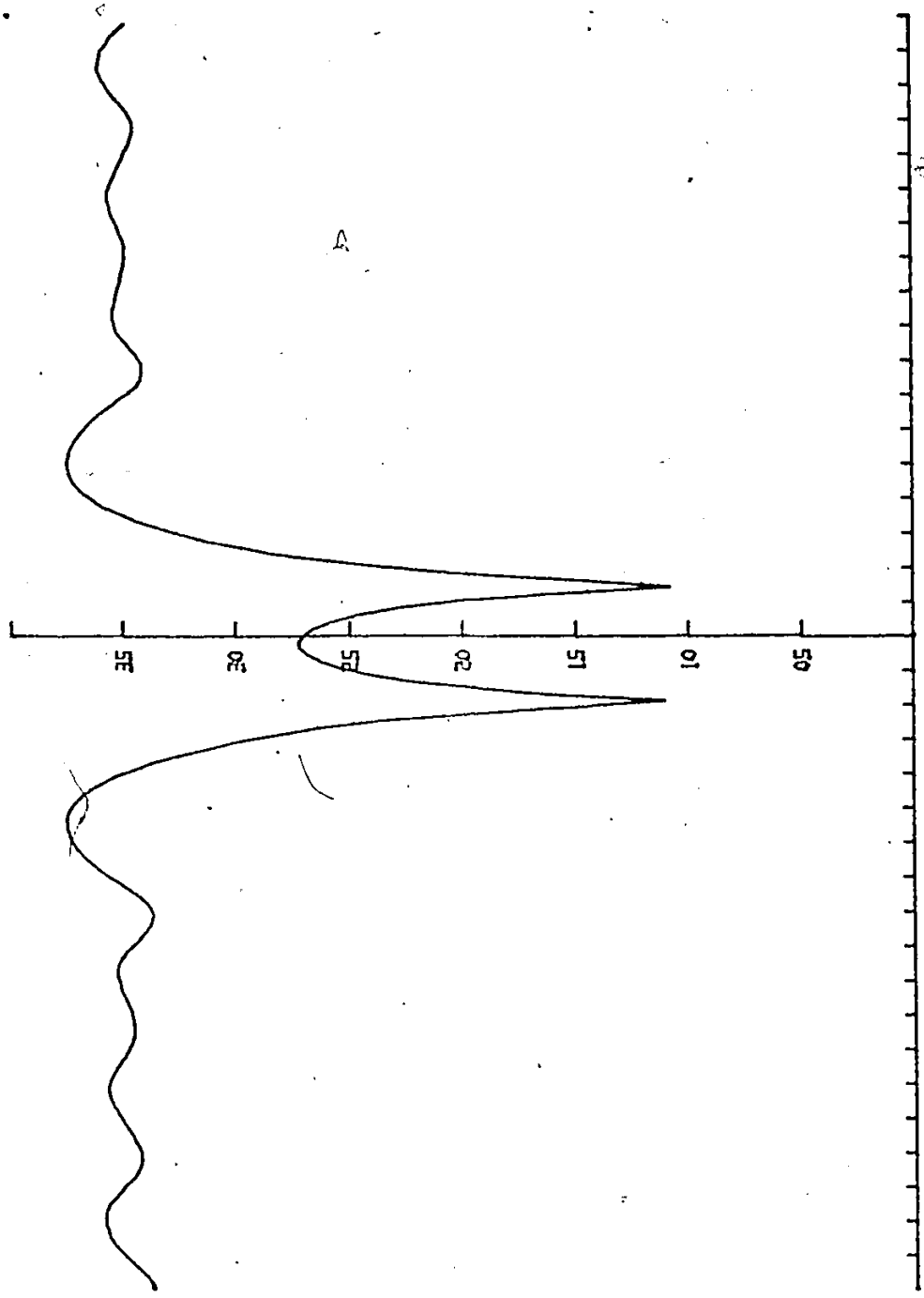

Figure 37: Scattering from 3 cm polyethylene disk, D=110cm, f=10.2GHz

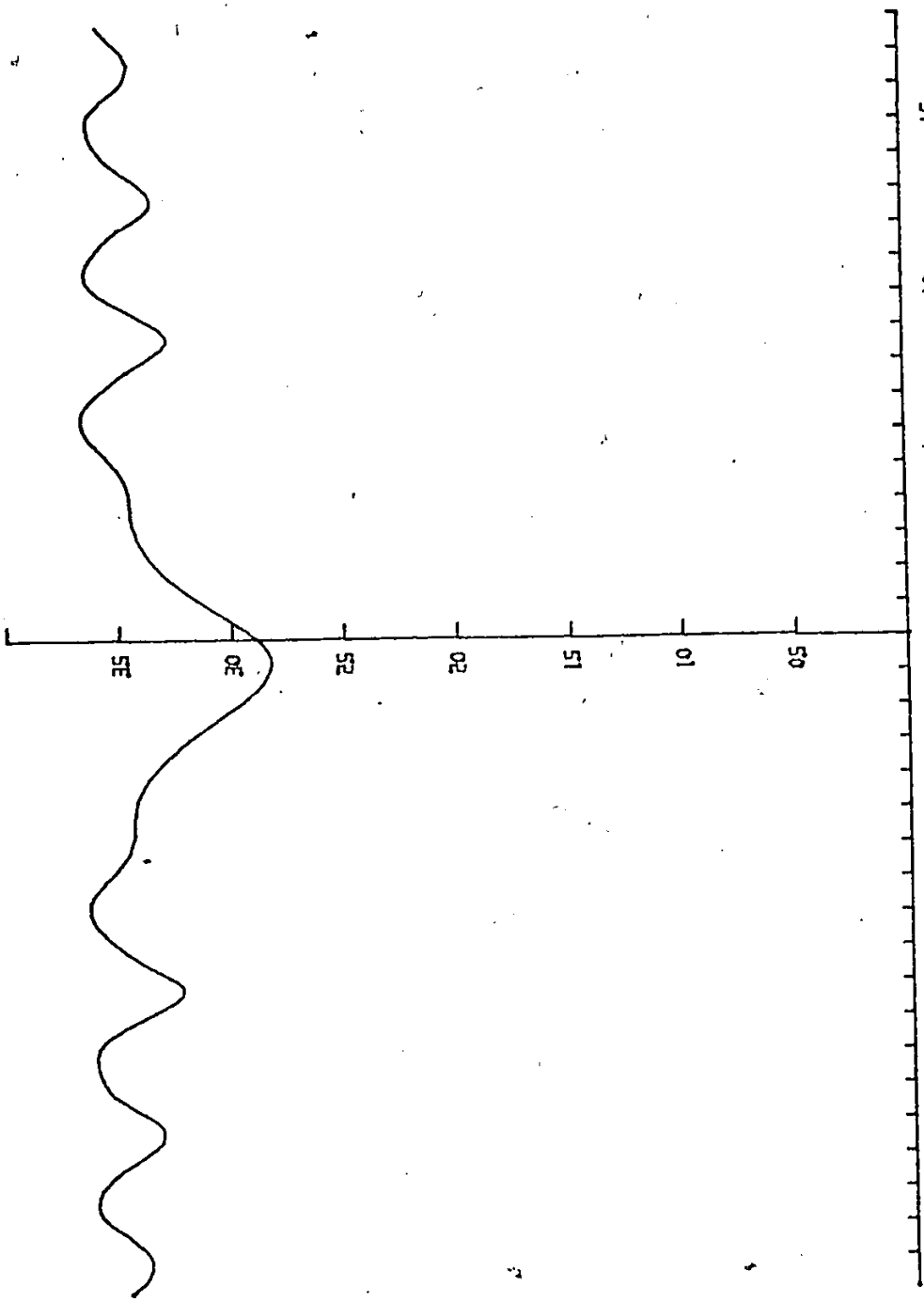

Figure 38: Scattering from 3cm fat phantom disk,D=110cm,f=10.2GHz

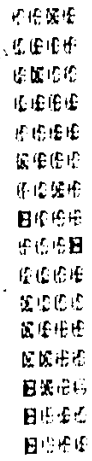

a) Reconstruction using unconstrained multiplicative ART.

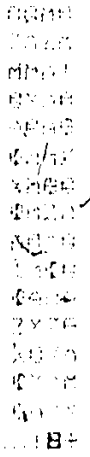

b) Same as a) but with 3% gaussian noise added to data.

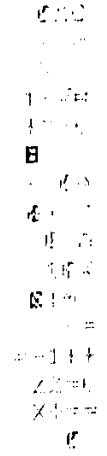

c) Same as a) but with 10% gaussian noise added to data.

Figure 39: Reconstruction of 4 pixel wide "bar" with 3 levels of AGN

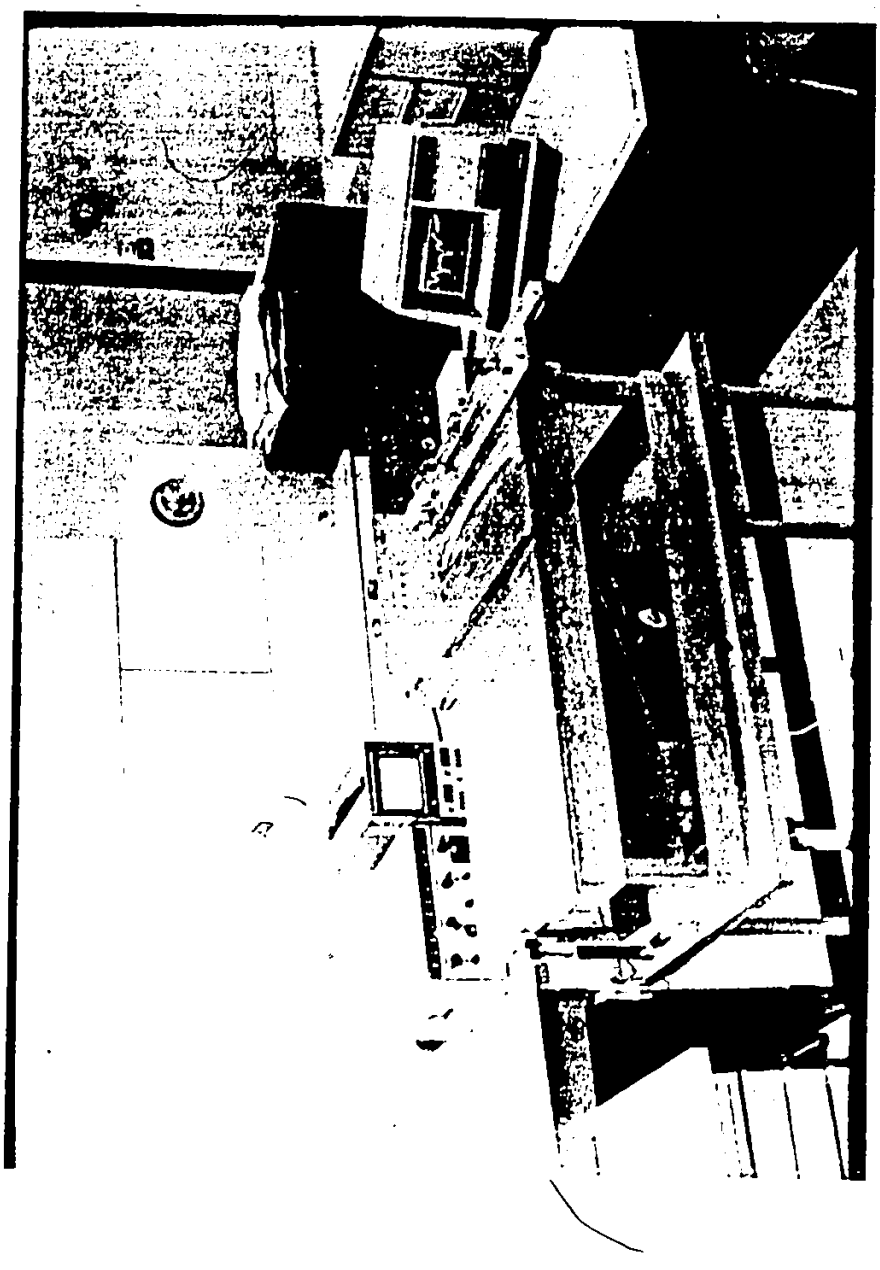

Figure 40: Photograph of the MCT-I System

REFERENCES

1. Anderson A.P., "Microwave Holography", Proc. IEE, Vol. 124, No. 11R, Nov. 1977. pp. 946-962.

2. Barber P.W. et al., "Electromagnetic Absorption in a Multilayered Model of Man", IEEE Trans. on Biomed. Eng., Vol. BME-26, No. 7, July 1979,pp. 400-405.

3. Basset H.L. et al., "New Techniques for Implementing Microwave Biological Exposure Systems", IEEE Trans. on Microwave Theory and Tech., Vol. MTT-19, No. 2, February 1971, pp.197-204.

4. Boerner W.M. and H.P.S. Ahluwala, "On a set of continuous wave electromagnetic inverse scattering boundary conditions", Can. J. Phys., V.50, No. 234, December 1, 1972, pp. 3023-3061.

5. Boyd D.P. et al., "Engineering Status of Computerized-Tomographic Scanning", SPIE Vol. 96 Optical Instrumentation in Med., 1976, pp.303-312.

6. Bracewell R.N., "Strip Integration in Radio Astronomy", Aust. J. Phys., Vol. 9, 1956, pp.198-217.

7. Brooks R. and Giovanni Di Chiro, "Principles of Computer Assisted Tomography (CAT) in Radiographic and Radioisotopic Imaging", Phys. in Med. and Biol., Vol. 21, No. 5,1976, pp.689-732.

8. Collins R.E., "Foundations of Microwave Engineering", Mcgraw-Hill, pp.259-263.

9. Cormack A.M., "Representation of a Function by its Line Integrals, with some Radiological Applications", J. Appl. Phys., Vol. 34, No. 9, September 1963, pp.2722-2727.

10. Davis D.T. et al., "Analysis of Electromegnetic Wave Probing for Undergrcund Voids", Lawrence Livermore Lab report #UCRL-52214, Jan 24, 1977.

11. Dines K.A. and R.J. Lytle, "Iterative Reconstruction of Undergrcund Refractive Index Distribution from Cross-Borehole Transmission Data", Lawrence Livermore Lab report #UCRL-52348, November 2,1977.

12. Ermert H. and R. Karg, "Multifrequency Acoustical Holography", IEEE Trans on Sonics and Ultrasonics, Vol. SU-26, No. 4, July 1979, pp.279-286.

13. Gilbert P.F.C., "The Reconstruction of a Three Dimensional Structure from Projections and its Application to Electron Microscopy II:Direct Methods", Proc. Roy. Soc. Lond, Vol 182, 1972, pp.89-102.

14. Gilbert B.K. et al., "Ultra-High Speed Transaxial Image Reconstruction of the Heart, Lungs and Circulation via Numerical Approximation Methods and Optimized Processor Architecture", Computers and Biomedical Research, Vol. 12, 1979, pp.17-38.

15. Gordon R., "A Tutorial on ART", IEEE Trans. on Nuclear Science, Vol. NS-21, June 1974, pp.78-92.

16. Greenleaf J.F. et al., "Algebraic Reconstruction of Spatial Distributions of Acoustic Velocities in Tissue from their Time of Flight", Acoustic Holography, Vol. 6, 1975, Plenum Press, N.Y., pp.71-90.

17. Gregg E.C. et al., "Microwave Radiation in Cancer Diagnosis-Transmission", Scientific Exhibit at AAPM Annual Meeting, Atlanta Georgia, Aug 1979.

18. Herman G.T. et al., "Rapid Computerized Tomography", Med. Data Processing, 1976, pp.582-598.

19. Herman G.T. and S.W. Rowland, "Three Methods for Reconstructing Objects from X-Rays: A Comparative Study", Computer Graphics and Image Processing, Vol.2, 1973, pp.151-178.

20. Hounsfield G.N., "Computerized Transverse Axial Scanning (Tomography) Part I. Description of System", British Journ. of Radiology, Vol. 46, 1973, pp.1016-1022.

21. Imbraile W.A. and R. Mittra, "The Two-Dimensional Inverse Scattering Problem", Trans. on Ant. and Prop, Vol. AP-18, No. 5, Sept. 1970, pp.633-642.

22. Johnson S.A. et al., "Reconstruction of Three Dimensional Velocity Fields and Other Parameters by Acoustic Ray Tracing", Ultrasonics Symposium Proc, 1975, pp.46-51.

23. Johnson C.C. and A.W. Guy, "Non Ionizing Electromagnetic Effects in Biological Materials and Systems", Proc. IEEE, Vol. 60, No.6, June 1972, pp.692-696.

24. Kak A.C., "Computerized Tomography with X-Ray, Emission and Ultrasound Sources", Proc. of the IEEE, Vol. 67, No. 9, September 1979, pp.1245-1272.

25. King R.W.P. and T.T. Wu, "The Scattering and Diffraction of Waves", Harvard University Press, Cambridge, Massachusets, 1959.

26. Kodis R.D., "Diffraction Measurements at 1.25 Centimeters", J. of Appl. Physics, Vol. 23, No. 2, February 1952, pp.249-255.

27. Larsen L.E. and J.H. Jacobi, "Microwave scattering parameter imagery of an isolated canine kidney",Med. Phys., Vol. 6, No. 5, Sept/Oct 1979, pp.394-403.

28. Lytle R.J. et al., "Using Cross-Borehole Electromagnetic Probing to Locate a Tunnel",Lawrence Livermore Lab report #UCRL-52166, October 21, 1976.

29. Mersereau R.M., "Recovering Multidimensional Signals from their Projections", Computer Graphics and Image Proc., Vol. 1, 1973, pp.179-195.

30. Mittra R. et al., "Transform Approach to Electromagnetic Scattering", Proc. IEEE, Vol. 67, NO. 11, Nov 1979, pp.1486-1503.

31. Mueller R.K. et al., "Reconstructive Tomography and Applications to Ultrasonics", Proc. of IEEE, Vol. 67, No. 4, April 1979, pp.567-587

32. Row R.V., "Microwave Diffraction Measurements in a Parallel-Plate Region", J. Appl. Physics, Vol. 24, No. 12, December 1953, pp.1448-1452.

33. Scudder H.J., "Introduction to Computer Aided Tomography", Proc. IEEE, Vol. 66, June 1978, pp.628-637.

34. Waggener R.G. and W.D. McDavid, "Computed Tomography", Advances in Biomedical Engineering, Vol. 7, April 1979, pp.65-100.

35. Zaklad H., "Computerized multiple X Rays give a view of the Body's Interior", Electronics, Oct. 1976, pp. 89-94.